

A PCA-based framework for determining remotely-sensed geological surface orientations and their statistical quality

Daven P. Quinn¹ and B.L. Ehlmann^{1,2}

¹Division of Geological and Planetary Sciences, California Institute of Technology, Pasadena, California, USA davenquinn@alumni.caltech.edu

²Jet Propulsion Laboratory, California Institute of Technology, Pasadena, California, USA

February 28, 2019

This preprint manuscript is under second-round review at Earth and Space Sciences.
Initial submission: May 2018

Abstract

The orientations of planar rock layers are fundamental to our understanding of structural geology and stratigraphy. Remote-sensing platforms including satellites, unmanned aerial vehicles (UAVs), and LIDAR scanners are increasingly used to build three-dimensional models of structural features on Earth and other planets. Remotely-gathered orientation measurements are straightforward to calculate but subject to uncertainty inherited from input data, differences in viewing geometry, and the regression process, complicating geological interpretation. Here, we improve upon the present state of the art by developing a generalized means for computing and reporting errors in strike-dip measurements from remotely sensed data. We outline a general framework for representing the error space of uncertain orientations in Cartesian and spherical coordinates and develop a principal-component analysis (PCA) regression method which captures statistical errors independent of viewing geometry and input data structure. We also build graphical techniques to visualize the uniqueness and quality of orientation measurements, and a process to increase statistical power by jointly fitting bedding planes under the assumption of parallel stratigraphy. These new techniques are validated by comparison of field-gathered orientations with minimally-processed satellite imagery of the San Rafael Swell, Utah and UAV imagery from the Naukluft Mountains, Namibia. We provide software packages supporting planar fitting and visualization of error distributions. This method provides a means to increase the precision and comparability of structural measurements gathered using a new generation of remote-sensing techniques.

Key Points

- A new statistical framework allows the error analysis of orientations of geologic planes and visualization of errors.
- Principal component analysis flexibly responds to different sources of error and supports joint fitting of parallel sedimentary bedding.
- The software workflow supporting error analysis and visualization can be used with terrestrial and planetary data at a variety of scales.

Contents

1	Introduction	3
2	Background: the structure of a remotely-sensed plane and its error space	5
3	Methods	7
3.1	PCA for planar fitting	7
3.1.1	Error treatment in OLS vs. PCA	7
3.1.2	Orientation examples	10
3.2	The nominal plane in PCA	12
3.2.1	Notation	12
3.2.2	Finding principal components	12
3.2.3	Rotation into a principal-component aligned frame	12
3.2.4	Strike and dip of the nominal plane	14
3.3	Confidence intervals for planar orientations	14
3.3.1	Eigenvectors as regression parameters	16
3.3.2	Errors limited by data variance	17
3.3.3	Population fit parameters	17
3.3.4	Errors to eigenvectors	19
3.3.5	Statistical error scaling	23
3.4	Displaying orientation error surfaces	23
3.4.1	Projection to hyperbolic errors	23
3.4.2	Spherical representation of errors	24
3.4.3	Maximum and minimum angular errors	25
3.5	Joint fitting of parallel bedding planes	25
4	Method demonstration and performance	27
4.1	Orbital imagery of the San Rafael Swell, Utah	27
4.1.1	Datasets	29
4.1.2	Orbital and field data comparison	29
4.2	UAV photogrammetry in the Naukluft Mountains, Namibia	31
4.2.1	Datasets	31
4.2.2	UAV and field data comparison	33
5	Potential future improvements to the statistical framework	35
5.1	Modeling data with different error structures	35
5.1.1	Adding a noise floor	35
5.1.2	Rescaling error sensitivity	35
5.1.3	Applying other statistical models	36
5.2	The link with Bingham statistics	36
6	Conclusion and recommendations	37
7	Acknowledgements	38

Bibliography	39
Appendices	42
A Quadric representation of the orientation error space	42
A.1 A hyperboloid enclosing the plane	43
A.2 Errors to normal vectors	43
A.3 General method to map a quadric to a conic	44
A.4 General method to move to spherical coordinates	45
B Software tools	45
Table 1 Classification of dataset major axes	8
Table 2 Data for orientation examples	11
Table 3 Summary of notation	13
Figure 1 Nominal plane schematic	6
Figure 2 Spherical errors schematic	6
Figure 3 Comparison of OLS and PCA regression	9
Figure 4 Context maps of highlighted attitudes	10
Figure 5 Comparisons of error distributions	15
Figure 6 Mean vs. Variance	18
Figure 7 Spherical projection of errors	20
Figure 8 Grouped Plane	26
Figure 9 San Rafael Swell (map)	28
Figure 10 San Rafael Swell (quality filtering)	30
Figure 11 San Rafael Swell (comparison)	31
Figure 12 Onis Example (context)	32
Figure 13 Onis Example (results)	34
Figure 14 Conjugate conics	42
Figure 15 Software tools	46
Figure 16 Software process diagram	46

1 Introduction

The orientations of geological features such as faults, dikes, lava flows, and sedimentary beds record characteristics of deposition or emplacement, episodes of deformation, and relationships between bodies of rock. Idealized planes describing these features are common units of geological analysis. The orientations of these planes have most often been collected directly, using a field structural compass or surveying equipment. The increasing viability of high-resolution remote-sensing techniques has allowed three-dimensional imaging of geological features at sub-meter scale.

In field mapping by a structural geologist, directly-measured orientations (e.g. outcrop measurements with a pocket transit) have been considered sufficiently accurate that errors are not reported. Orientations measured using remotely-gathered data are a powerful new tool for geological analysis, especially when outcrops are inaccessible to direct measurement. However, poorly-modeled and hard-to-visualize errors complicate assessment of the true orientation of a geological structure. Remote-sensing datasets spatially vary in resolution and quality; measurements are additionally biased by terrain effects, sensor-dependent noise, measurement geometry, operator error in defining relevant features, and other factors.

Even carefully-planned structural studies with consistent error analysis procedures cannot be easily interpreted using current visualization tools. For instance, map symbols for nominal strike and dip do not provide a means of understanding commonly unpredictable, nonlinear errors inherent in orientation measurements in varied terrain. Individual orientation measurements often only coarsely correspond to the overall structural pattern (e.g. *Lewis and Aharonson, 2006; Okubo et al., 2008; Quinn and Ehlmann, 2018, submitted*). Without methods to visualize orientation errors, reported bedding orientations do not fully communicate information used in study interpretations.

One major motivation of this work is the orbital mapping of layered rocks on Mars, which are key indicators of Mars' geological history (e.g. *McEwen et al., 1999; Malin and Edgett, 2000; Quantin et al., 2005; Dromart et al., 2007; Lewis et al., 2008a; Stack et al., 2015*). For example, sedimentary deposits are mapped from orbit and with rovers, but detailed evaluation of their depositional mechanisms requires understanding bedding orientations, particularly bedding dip (e.g. *Lewis and Aharonson, 2006, 2014; Lewis et al., 2008b; Okubo et al., 2008; Okubo, 2010; Edgar et al., 2012; DiBiase et al., 2013; Kite et al., 2013; Goudge et al., 2017; Quinn and Ehlmann, 2018, submitted*). Detailed accounting for errors is also important in large-scale regional studies, where measurements are derived from multiple datasets and outcrops of varying quality (e.g. *Metz et al., 2010*).

At present, some Mars mapping studies report no error ranges for bedding orientations (e.g. *DiBiase et al., 2013*), while others report errors output from commercial regression packages (e.g. *Okubo et al., 2008*). Other studies use "dip error" (*Lewis and Aharonson, 2006; Goudge et al., 2017*),

38 “pole error” (*Kite et al.*, 2016), or bootstrap resampling statistics (*Metz et al.*, 2010; *Fraeman et al.*,
39 2013) to evaluate measurement quality. The varying approaches used to generate orientation
40 errors, with different degrees of reporting rigor, complicate understanding of the accuracy and
41 precision of specific strike/dip measurements and impede geologic interpretation.

42 The methods presented in this study were developed in conjunction with structural mapping
43 of the layered sulfates at northeast Syrtis Major, Mars. These thick layered deposits occupy a crit-
44 ical stratigraphic interval, but their relatively poor exposure complicates orientation measure-
45 ment. Additionally, because small changes in dip can imply completely different depositional
46 processes, high-confidence angular measurements are crucial drivers of interpretation (*Quinn and*
47 *Ehlmann*, 2018, submitted).

48 The use of remotely-sensed orientation measurements in terrestrial geology is also a key
49 driver of this work. High-resolution satellite imagery and digital elevation models (DEMs) now
50 available for much of the Earth’s surface (e.g. *Gesch et al.*, 2014) support regional photogeologic
51 mapping. The advent of field-portable Light Detection and Ranging (LIDAR) instruments (*Buck-*
52 *ley et al.*, 2008) and the improving accuracy of structure-from-motion (SfM) photogrammetry in-
53 creasingly allow remote measurement of geological surface orientations. Numerous recent stud-
54 ies use orientation measurements from unmanned aerial vehicle (UAV) photogrammetry (e.g.
55 *Vollgger and Cruden*, 2016), often using three-point analytical approximations (*Fienen*, 2005) or
56 commercial regression packages.

57 Terrestrial remote-sensing structural studies are hindered by the same data-quality and geo-
58 metric uncertainties that complicate such work on Mars. For example, in a recent study of the
59 relative quality of orientations extracted from different remote-sensing datasets, *Cawood et al.*
60 (2017) extract bedding planes and fold axes from LIDAR and SfM photogrammetric digital surface
61 models of weathered beds of the Stackpole syncline. Although most cases allowed high-accuracy
62 comparisons with direct measurements, significant differences in fit structure were found be-
63 tween LIDAR, ground-, and UAV-based photogrammetry. These discrepancies are related to the
64 orientation of the outcrop and viewing geometry as well as the scale of facet construction and
65 point fitting.

66 Improvements on the state-of-the-art in computing and visualizing orientation errors must
67 flexibly respond to different types of error. Bedding orientation measurements depend not only
68 on the internal errors of the remote-sensing dataset but also on the geometry of the outcrop
69 measured (e.g. hillslope concavity and aspect) and accuracy in following bedding features. Mea-
70 surements from the same dataset and geologic unit can have completely different error structures
71 depending on the shape of topography, presenting a challenge for error analysis. A flexible statis-
72 tical and error-visualization approach for planar orientation measurements will enable quantita-
73 tive comparison between planar fits with completely different error structures. By increasing the
74 robustness of orientation determination from heterogeneous data, such a framework will extend

75 the range of situations in which structural metrics can be reliably assessed from remote-sensing
76 imagery, enabling statistically rigorous comparison of measurements with variable source data
77 type, outcrop exposure and quality, and viewing geometry.

78 In this contribution, we detail a novel method for the calculation and visualization of geolog-
79 ical orientation errors. First, we describe a generalized approach to planar orientation errors for
80 three-dimensional datasets [Section 2] and its implementation as a PCA-based statistical proce-
81 dure for planar fitting [Section 3]. We test the method using terrestrial orientations recovered
82 from satellite and UAV data [Section 4] and discuss potential alternative statistical parameteri-
83 zations [Section 5]. Finally, we describe general geometric transformations for the error space of
84 a plane A and two complimentary open-source software packages that support planar fitting and
85 error visualization B.

86 **2 Background: the structure of a remotely-sensed plane and its error** 87 **space**

88 A geologic surface is typically extracted from remote-sensing data by isolating representative
89 points from a three-dimensional surface or outcrop model. Commonly, a bedding trace is dig-
90 itized from visible imagery and the elevations of constituent points are extracted from a coreg-
91 istered gridded DEM. Related procedures include the grouping closely-spaced LIDAR points that
92 sample the same surface (e.g. *Weingarten et al.*, 2004) or targeted elevation measurement along
93 a feature trace by theodolite or differential GPS. Since remote-sensing datasets are typically de-
94 fined in Cartesian spatial coordinates, all of these methods produce an array of three-dimensional
95 points in space that collectively represent a single feature.

96 Planar representations of geological surfaces are typically modeled using regression statistics:
97 the set of coordinates representing a potential plane is converted to an orientation by finding the
98 best-fitting plane through the dataset using minimization (e.g. PCA, OLS, and other regression
99 frameworks) in Cartesian coordinate space (*Fahrmeir et al.*, 2013; *Jolliffe*, 2002). The idealized
100 geologic surface that results from regression can be mathematically described as a plane, requir-
101 ing three free parameters. Description of orientation alone requires only two free parameters,
102 represented either as slopes in two directions or the orientation of a normal vector to the plane
103 [Figure 1a].

104 Regression of a best-fitting plane inherently involves uncertainty, which combines with irreg-
105 ularities in the input dataset to produce orientation errors. In Cartesian space terms, these errors
106 can be represented as a hyperboloid of two sheets enclosing all possible planes in the dataset, vary-
107 ing around the nominal regression line, or alternatively as a set of normal vectors perpendicular
108 to the plane. Assuming a fixed length, the error space for this normal vector forms an ellipsoid
109 containing possible vector endpoints [Figure 1b].

110 In spherical coordinates, orientations are intuitively represented as a pair of angles (com-

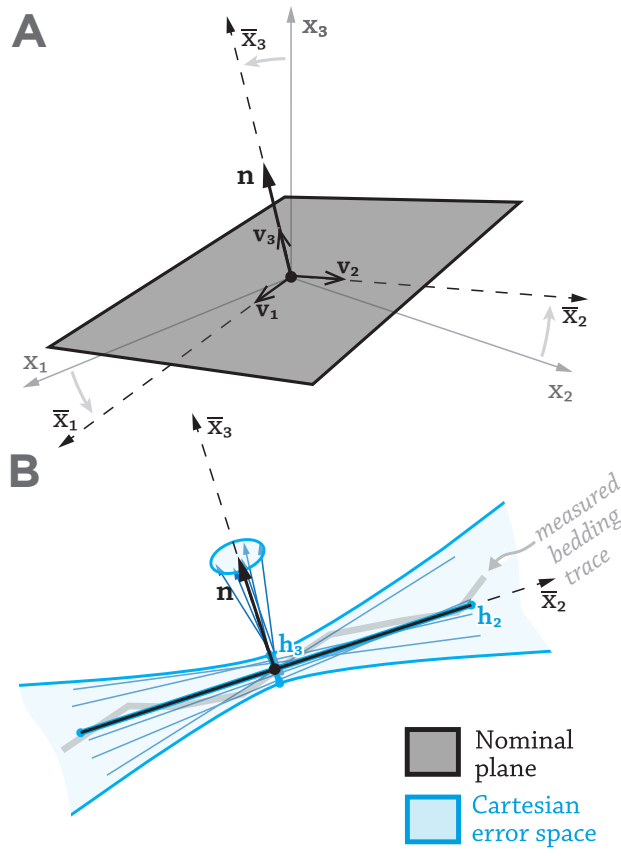


Figure 1: Schematic representation of the structure of a plane with errors and its relation to the global Cartesian coordinate system \mathbf{x} . (a) The plane and its associated normal vector \mathbf{n} . In unweighted PCA, \mathbf{n} falls along the principal component axis \bar{x}_3 . The three unit vectors \mathbf{v}_i , oriented along \bar{x}_i , form rows of the rotation matrix \mathbf{V} that maps \mathbf{x} to $\bar{\mathbf{x}}$. (b) A \bar{x}_2 - \bar{x}_3 slice of the nominal plane and its normal vector, along with a bundle of planes with slightly different orientations and the encompassing hyperbolic error space (blue).

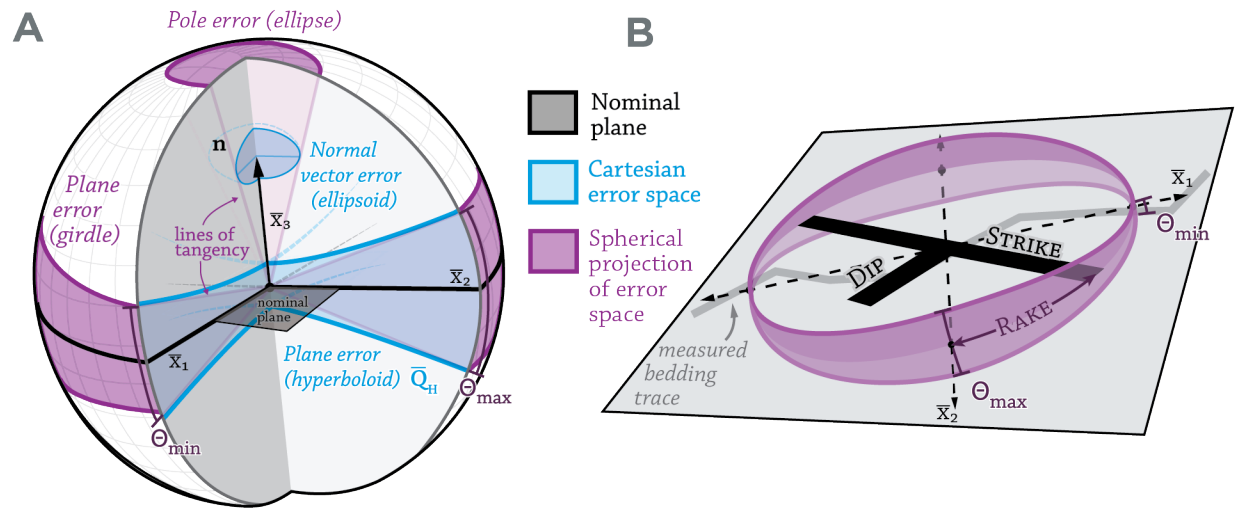


Figure 2: Schematic representation of the relationship between the nominal planar fit (black), the hyperbolic error shell \bar{Q}_H and inverse ellipsoid representing the normal vector endpoint (blue), and the spherical error distribution formed by projecting the tangents to these error spaces onto the unit sphere (purple). θ_{\min} and θ_{\max} define the scale of orientation errors along two axes within the plane, \bar{x}_1 and \bar{x}_2 . (a) Projection of Cartesian error space to spherical coordinates, both as a planar girdle and pole error ellipse. (b) Orientation of the error space to the plane (defined by θ_{\min} and θ_{\max}) relative to the nominal plane, emphasizing the rake angle needed to report the directions of errors within the plane.

111 monly, strike/dip, or dip/dip-direction). This two-angle representation supports visualization
112 of orientation information on stereonet and related spherical plots. Previous studies of bed-
113 ding orientation errors have parameterized orientation error in terms of strike and dip (*Cruden*
114 *and Charlesworth, 1976*), and many workers have reported orientation errors in these terms (e.g.
115 *Lewis and Aharonson, 2006; Okubo et al., 2008*). However, orientation errors are not necessarily
116 aligned with the strike/dip parameters that describe the nominal plane; errors expressed in these
117 terms rely implicitly on the small-angle assumption. Near-horizontal bedding (a common mode
118 of stratigraphic exposure) has highly nonlinear angular dispersion in strike when approaching
119 zero dip, with large covariances between the two.

120 Errors parameterized as pole error (angular error around the nominal orientation of a plane)
121 operates in spherical coordinates, entirely avoiding the issues of linearization. Directional statis-
122 tical fitting mechanisms commonly used for geological orientations yield errors parameterized as
123 pole error but operate entirely on data already expressed in angular terms (e.g. *Bingham, 1974;*
124 *Onstott, 1980; Kent et al., 1983; Fisher et al., 1987; Mardia, 2014*). For data defined in Cartesian
125 space, the structure of these pole errors must be defined with a statistical process.

126 Regression errors defined in Cartesian space can be mapped to spherical coordinates using
127 geometric projection. Error spaces to a planar fit in Cartesian coordinates can be projected on a
128 unit sphere: the hyperbolic errors to the nominal plane map to a spherical girdle (a bundle of great
129 circles), and the cone of normal vector errors projects to an ellipse, a two-axis expression of the
130 “pole error” [Figure 2a]. The angular span of this spherical girdle or ellipse can be defined by θ_{\max} ,
131 the maximum angular error to the plane, and θ_{\min} , which is orthogonal to θ_{\max} by definition. θ_{\max}
132 need not be oriented along strike or along dip; instead, the orientation of θ_{\max} with respect to the
133 nominal plane is expressed using a *rake* angle between the strike of the plane and θ_{\max} [Figure 2b].
134 This format generalizes pole error to allow the full expression of a Cartesian orientation error
135 space in angular terms, with five free parameters. Errors expressed in this structure are the target
136 of this work.

137 **3 Methods**

138 **3.1 PCA for planar fitting**

139 **3.1.1 Error treatment in OLS vs. PCA** Ordinary least-squares (OLS) regression is the most com-
140 mon technique for fitting orientations of lines and planes. However, many other regression tech-
141 niques exist which chiefly differ in their mechanism for apportioning error along the coordinate
142 axes of the fit. Many of these parameterizations can be used to define errors to a plane.

143 OLS regression fundamentally tests the relationship of a dependent variable with a set of
144 independent variables. All error is assumed to belong to the dependent variable, which in spatial
145 data is usually assigned to the vertical plane. This property inhibits the fitting of steep slopes
146 [Figure 3]. Geological planes are often expected to be steeply dipping, depending on their origin

Table 1: Classification of dataset major axes

Scenario ^a	Hyperbolic axes ^b	Shape of variance ellipsoid	Notes
A	$h_1 \approx h_2 > h_3$	Prolate ellipsoid	Plane well-defined in two dimensions, with small error axis
B	$h_1 > h_2 > h_3$	Scalene ellipsoid	Quality of planar fit depends on axial dimensions and structure of dataset
C	$h_1 > h_2 \approx h_3$	Oblate ellipsoid	Defined along a line, but with no unique planar orientation
D	$h_1 \approx h_2 \approx h_3$	Spherical	Poorly constrained on all axes, no clear plane defined

^a Scenario lettering corresponds to Figures 4, 5, and 7.

^b $\mathbf{h} = \boldsymbol{\lambda}$ in *Onstott* (1980), and $\mathbf{h} = \boldsymbol{\lambda} + F\boldsymbol{\sigma}_\lambda$ in this work (see Table 3 for notation definition).

147 and geologic context, and it is not always reasonable to assume that errors are chiefly vertical.

148 Instead of OLS, this study focuses on principal component analysis (PCA). PCA fits errors
 149 along all axes simultaneously, with no distinction between independent and dependent data; er-
 150 rors are minimized on an axis orthogonal to the best-fitting plane. The flexibility of this fitting
 151 mechanism is a significant advantage for fitting arbitrarily-oriented planes atop datasets with
 152 different error structures; it is particularly relevant when errors are known to be non-vertical.

153 Many such situations exist for geological orientation measurements: errors for photogram-
 154 metric datasets are generally dependent on the viewing geometry of the image pair(s) used to
 155 assemble the 3D model; elevation models created from oblique UAV imagery of cliff faces [e.g.
 156 Section 4.2] will have chiefly horizontal errors, and multi-view SfM datasets will have errors ori-
 157 ented along arbitrary, oblique view planes. Even elevations measured on a gridded dataset have
 158 several sources of non-vertical error: (1) error in the construction of the DEM (e.g. photogram-
 159 metric image-registration error), (2) resampling error (sub-post smoothing imparted by gridding)
 160 (3) sampling error (inexact digitization of measured features), and (4) downslope bias. Though
 161 often poorly quantified, these errors still influence the output of planar fitting. PCA has been
 162 used for orientation measurement in contexts requiring flexibility in the expected orientation of
 163 features, ranging from paleomagnetism data reduction (*Kirschvink*, 1980) to computer vision and
 164 scene-mapping (*Weingarten et al.*, 2004; *Nurunnabi et al.*, 2012).

165 Much of the literature urges caution when applying PCA to estimate statistical confidence
 166 (e.g. *Faber et al.*, 1993, 1995; *Jolliffe*, 2002). PCA is not usually developed or motivated with a
 167 clear probabilistic framework (*Tipping and Bishop*, 1999); instead, it is commonly used for dimen-
 168 sionality reduction, compressing the variation of a multidimensional dataset into a smaller set
 169 of explanatory variables. That process is difficult to statistically model, largely limiting PCA to
 170 algorithmic applications (e.g. image processing) and exploratory data analysis, except where ex-

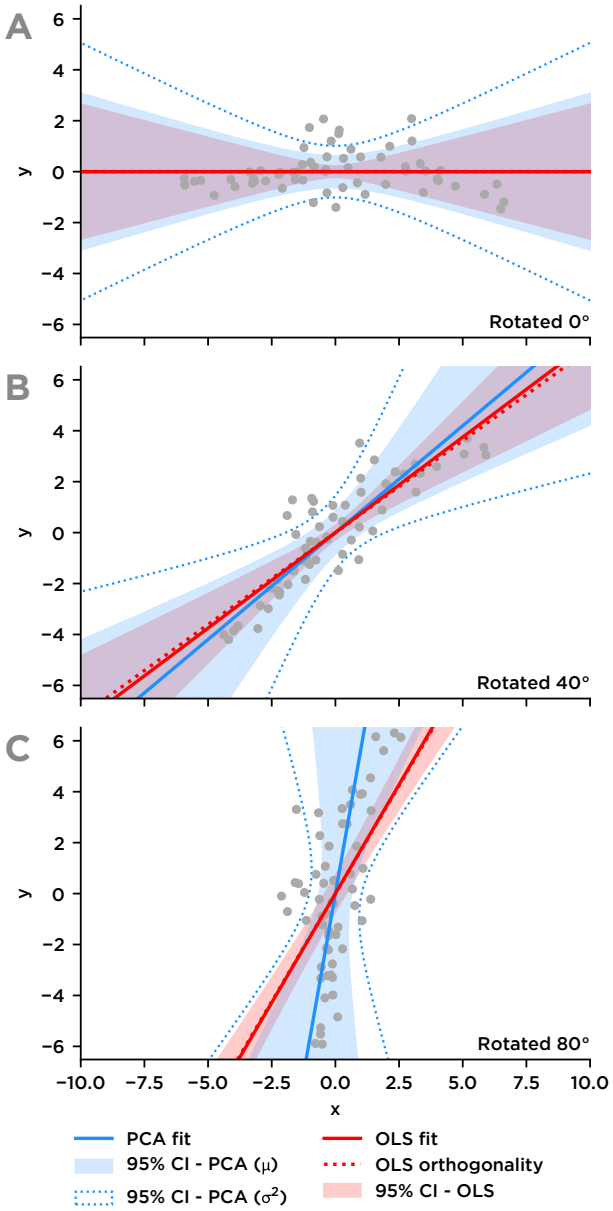


Figure 3: PCA and OLS regressions of a 2-dimensional, zero-centered point cloud rotated counterclockwise by (a) 0°, (b) 40°, and (c) 80°, emphasizing the nonlinear relationship between OLS and PCA regressions for differently-dipping planes with the same measurement scatter. Unweighted PCA retains the same error structure regardless of orientation, while the scale of OLS errors decrease as fitted orientations steepen. OLS is also structurally unwilling to fit near-vertical data. When it is not rigorously known that errors occur only in the vertical plane, PCA provides more potential to reconstruct orientation data.

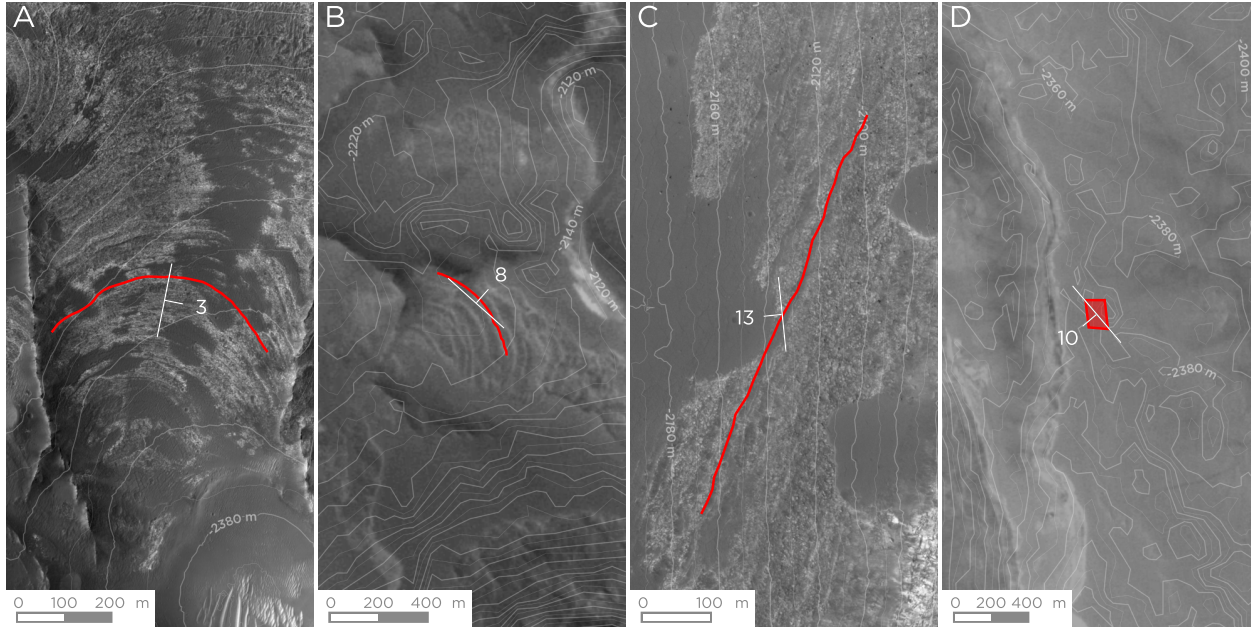


Figure 4: Context maps showing traced bedding planes (red) and nominal calculated bedding orientations for four orientation measurements in the NE Syrtis region of Mars. Imagery backdrop is HiRISE or CTX imagery, and 10 m contours derived from photogrammetry on the same dataset show the elevation data used to extract orientations. (a) a bedding exposure on a concave hillslope between two parallel raised ridges, atop a HiRISE image and elevation model. (b) A similar concave hillslope with slightly less 3D exposure, atop lower-resolution CTX data. (c) A linear bedding trace on a planar, west-facing hillslope. (d) A rectangular area of a dipping lava flow surface atop low-precision CTX topography.

171 plicit statistical rationale can be advanced for how many principal components to retain (*Jolliffe*,
 172 2002). For fitting spatial planes, both input and output data are tied to orthonormal spatial coord-
 173 inates. Thus, finding the best-fitting plane involves only rotation, not dimensionality reduction,
 174 allowing us to circumvent this source of uncertainty. Evaluating the orientation and scatter along
 175 the axes of the input data, rather than discarding some of them, is statistically straightforward
 176 [Section 3.3].

177 **3.1.2 Orientation examples** To exhibit the properties of the PCA algorithm applied to datasets of
 178 varying quality, we focus on four endmember examples of digitized bedding traces [Figure 4] with
 179 a range of dataset structures of types discussed in Table 1. These examples are digitized traces
 180 of sedimentary bedding measured within an area in NE Syrtis, Mars during the study described
 181 in *Quinn and Ehlmann* (2018). Orientations were collected atop paired orthophotos and DEMs,
 182 which have varying spatial resolution and error structure due to differences in dust cover and
 183 stereo geometry. These bedding traces have different potential error structures due to their range
 184 of hillslope aspect and curvature. We follow these bedding traces through transformation of their
 185 error space from Cartesian to spherical coordinates; the numerical breakdown of their errors is
 186 summarized in Table 2.

Table 2: Data for orientation examples

n	L^1	R^2	Eigenvalues			Spherical summary (°)				
			λ_1	λ_2	λ_3	strike	dip	rake	θ_{\min}	θ_{\max}
Type examples [Table 1, Figures 5 and 7, ordered a-d]										
31	479	2.0	17228	422.9	0.82	311.7	7.6	81.5	0.59	3.88
546	584	1.1	21634	2079.3	0.11	11.3	3.5	172.7	0.15	0.48
593	615	2.4	31514	10.0	0.66	174.2	13.2	60.9	0.29	16.49
172	0	18.5	2163	948.1	73.74	139.6	10.1	119.2	13.17	19.92
Joint fitting of parallel planes [Figure 8]										
<i>Well-constrained single-bed measurements</i>										
476	507	0.7	16825	1437.8	0.09	9.3	3.5	9.9	0.15	0.51
546	584	1.1	21634	2079.3	0.11	11.3	3.5	172.7	0.15	0.48
<i>Joint fit</i>										
1217	–	1.3	6431	972.4	0.13	11.8	3.5	156.1	0.28	0.71
<i>Components (ordered from north to south)</i>										
315	332	0.5	8940	88.1	0.05	339.7	3.5	167.7	0.15	1.54
189	209	1.1	3544	14.1	0.09	38.3	6.7	112.5	0.34	5.43
367	389	0.9	12008	205.8	0.14	7.3	3.4	158.3	0.22	1.69
138	146	0.6	1746	5.7	0.06	358.1	6.1	70.7	0.43	7.69
208	217	0.3	3778	33.0	0.02	9.5	3.8	59.5	0.16	1.72

¹ L : length of bedding trace (m)² R : maximum residual to plane (m)

187 **3.2 The nominal plane in PCA**

188 **3.2.1 Notation** Matrices are uppercase and bold (\mathbf{M}), while vectors are lowercase and bold (\mathbf{x}).
189 Vector components use upright characters (x_1) while scalar quantities are in script (n). The sub-
190 script i defines a range of indices over the dimensions of the coordinate basis $i = [1, 2, 3]$. Thus
191 $\mathbf{x} = \mathbf{x}_i = [x_1, x_2, x_3]$. When a vector component is given in subscript (e.g. σ_λ), its implicit i
192 index is dropped. An index of all notation is contained in Table 3.

193 **3.2.2 Finding principal components** The original data matrix \mathbf{D} is a $n \times 3$ matrix containing
194 three-axis coordinates in a Cartesian coordinate system (commonly 3D geographical points in
195 UTM or another local geodetic system). n represents the number of independent observations
196 in the dataset. The centered data matrix \mathbf{M} is centered

$$\mathbf{M} = \mathbf{D} - \mu_{\mathbf{D}} \quad (1)$$

197 by subtraction of the mean along each axis. The sample covariance matrix is defined as

$$\mathbf{C} = \frac{1}{n-1} \mathbf{M}^T \mathbf{M}, \quad (2)$$

198 the cross-product matrix $\mathbf{M}^T \mathbf{M}$ scaled by the size of the dataset.

199 PCA is formally described as an eigenvector decomposition of \mathbf{C} , represented as

$$\mathbf{C} = \mathbf{V} \mathbf{\Lambda} \mathbf{V}^T \quad (3)$$

200 and arrived at by numerical optimization. \mathbf{V} is a rotation matrix composed of the eigenvectors,
201 $\boldsymbol{\lambda}$ is a vector of eigenvalues of \mathbf{C} , and $\mathbf{\Lambda} = \text{diag}(\boldsymbol{\lambda})$ is the diagonal matrix of eigenvalues. The
202 eigenvalues represent the variance of \mathbf{M} along each eigenvector row (\mathbf{v}_i) of \mathbf{V} .

203 In practice, singular value decomposition is used for a more numerically stable implementa-
204 tion of PCA. This technique is represented as

$$\mathbf{U} \mathbf{S} \mathbf{V}^T = \mathbf{M}, \quad (4)$$

205 where $\mathbf{U}^T \mathbf{U} = \mathbf{V}^T \mathbf{V} = \mathbf{I}$ and $\mathbf{S} = \text{diag}(\mathbf{s})$ is a diagonal matrix containing the singular values of
206 the data matrix \mathbf{M} . A direct relationship between the singular values and the eigenvalue matrix,

$$\mathbf{\Lambda} = \frac{\mathbf{S}^2}{n-1}, \quad (5)$$

207 allows recovery of the eigenvalues $\boldsymbol{\lambda}$.

208 **3.2.3 Rotation into a principal-component aligned frame** Geometrically, PCA corresponds to
209 rotation of the dataset into a decorrelated reference frame. The rotation matrix \mathbf{V} operates on

Table 3: Summary of notation

Symbol	Meaning	
i	In subscript, represents component of 3D vector basis (1,2 or 3)	
n	Number of samples in data matrix	
*	In subscript, represents all n samples in data matrix.	
\mathbf{x}, \mathbf{x}_i	Orthonormal basis vectors defining “world” coordinates	3×1
\mathbf{D}	Data matrix in “world” coordinates	$n \times 3$
$\boldsymbol{\mu}_D$	Column-wise mean of data matrix	3×1
<i>Principal component analysis</i>		
\mathbf{M}	Data matrix centered on all axes	$n \times 3$ $\mathbf{M} = \mathbf{D} - \boldsymbol{\mu}_D$
\mathbf{C}	Covariance matrix for \mathbf{M}	3×3 $\mathbf{C}(n-1) = \mathbf{M}^T \mathbf{M}$
$\boldsymbol{\lambda}, \lambda_i$	Vector of eigenvalues of \mathbf{M}	
$\boldsymbol{\Lambda}$	Diagonal matrix of eigenvalues of \mathbf{M}	$\boldsymbol{\Lambda} = \mathbf{I} \boldsymbol{\lambda}$
\mathbf{V}	Rotation matrix of orthonormal eigenvectors	3×3
\mathbf{v}_i	Eigenvector rows of \mathbf{V}	3×1
\mathbf{n}	Normal vector to the best-fitting plane	$\mathbf{n} = \mathbf{v}_3$
$\bar{\mathbf{x}}, \bar{\mathbf{x}}_i$	Orthonormal coordinate basis aligned with principal component axes \mathbf{v}_i	
$\bar{\mathbf{M}}$	Data matrix aligned with principal component axes	$\bar{\mathbf{M}} = \mathbf{M} \mathbf{V}^T$
<i>Singular value decomposition</i>		
\mathbf{U}	Left singular vectors of \mathbf{M}	$n \times 3$
\mathbf{S}	Diagonal matrix of the singular values of \mathbf{M}	eigenvalues of \mathbf{C}
\mathbf{s}, s_i	Vector of singular values	$\mathbf{s} = \sqrt{\boldsymbol{\lambda}}(n-1)$
<i>Statistical error analysis</i>		
$\sigma_{\bar{\mathbf{M}}}$	Standard error of data matrix	$\sigma_{\bar{\mathbf{M}}} = \sqrt{\boldsymbol{\lambda}} = \frac{\mathbf{s}}{\sqrt{n-1}}$
$\sigma_{\boldsymbol{\lambda}}$	Standard error of the eigenvalues	
$\hat{\boldsymbol{\beta}}$	Sample regression parameters	2×1
d	Degrees of freedom of the estimator	$d = 2$ for angular error analysis
α	Confidence level for an error surface	$\alpha = 0.95$ is typical
$F_{\alpha,d,n-d}$	Fisher percent-point test statistic	
<i>Construction of error surfaces</i>		
\mathbf{p}	Parameters of the nominal plane in $\bar{\mathbf{x}}$	$\mathbf{p} = \boldsymbol{\lambda}$
\mathbf{e}	Errors to the nominal plane in $\bar{\mathbf{x}}$	$\mathbf{e} = \text{error}(\boldsymbol{\lambda}) = F_{\alpha,d,n-d} \sigma_{\boldsymbol{\lambda}}$
\mathbf{h}	Semimajor axes of hyperbolic quadric defining an error surface	$\mathbf{h} = \mathbf{p} + \mathbf{e}$
\mathbf{Q}	Matrix representation of a quadric surface	5×5 as defined in text
$\bar{\mathbf{Q}}_{\mathbf{H}}$	Tensor representation of a hyperbolic error quadric for semiaxes \mathbf{h}	
\mathbf{T}	An affine or projective transformation matrix	as defined in text
$\mathbf{C}_{\mathbf{H}}$	Matrix representation of conic section	4×4 as defined in text
<i>Spherical errors</i>		
γ	Angle in $[0, 2\pi]$ from $\bar{\mathbf{x}}_1$ within $\bar{\mathbf{x}}_{1,2}$ plane	
$\bar{\mathbf{x}}_{\gamma}$	2D coordinate basis orthogonal to nominal plane, defined by $\bar{\mathbf{x}}_{\gamma}, \bar{\mathbf{x}}_3$	
θ_{γ}	Angular error for an arbitrary direction within the plane	
$\theta_{\max}, \theta_{\min}$	Maximum and minimum angular errors at $\gamma_{\min} = 0, \gamma_{\max} = \frac{\pi}{2}$	

210 the covariance matrix \mathbf{C} to eliminate cross-correlations between components, defining a new
 211 coordinate basis aligned with the directions of maximum variability of the dataset. This rotated
 212 orthonormal coordinate basis, $\bar{\mathbf{x}}$, is aligned with the axes of \mathbf{V} [Figure 1]. An arbitrary vector \mathbf{a}
 213 in the global Cartesian plane can be rotated into this coordinate system using $\bar{\mathbf{a}} = \mathbf{a} \mathbf{V}^T$.

214 Rotation of data into a principal-component aligned coordinate basis significantly eases error
 215 analysis and visualization of the structure of the dataset relative to its best-fitting plane. The
 216 “axis-aligned” projection of the input dataset $\bar{\mathbf{M}}$, defined as $\bar{\mathbf{M}} = \mathbf{M} \mathbf{V}^T$, collapses the dataset
 217 onto its best-fitting plane. Inverting Equation 3, the sample covariance matrix \mathbf{C} can be expressed
 218 in this coordinate system as

$$\bar{\mathbf{C}} = \mathbf{\Lambda} = \boldsymbol{\lambda} \mathbf{I} = \mathbf{V}^T \mathbf{C} \mathbf{V}. \quad (6)$$

219 The rotated dataset $\bar{\mathbf{M}}$ varies independently along each axis of $\bar{\mathbf{x}}$, and the magnitude of the
 220 eigenvalues $\boldsymbol{\lambda}$ of the PCA fit is proportional to the scale of the dataset along each principal com-
 221 ponent axis. The eigenvalues are equivalent to the three-component vector variance of the decor-
 222 related data along each axis of $\bar{\mathbf{x}}$:

$$\boldsymbol{\lambda} = \boldsymbol{\sigma}_{\bar{\mathbf{M}}}^2. \quad (7)$$

223 The axes \bar{x}_1 and \bar{x}_2 fall within the best-fitting plane through the dataset. \bar{x}_3 is along the nor-
 224 mal to the plane; scatter along this axis represents the error in the planar fit. Thus, the third
 225 column of the aligned data matrix, $\bar{\mathbf{M}}_{*,3}$, represents residuals from the nominal planar fit. Ro-
 226 tation of the dataset into $\bar{\mathbf{x}}$ provides a useful view of the distribution of residuals and potential
 227 nonrandom structure relative to the best-fitting plane: plotting $\bar{\mathbf{M}}_{*,1}$ vs. $\bar{\mathbf{M}}_{*,2}$ yields a view of
 228 structure within the model plane, and $\bar{\mathbf{M}}_{*,i}$ vs. $\bar{\mathbf{M}}_{*,3}$ for $i = 1, 2$ shows residuals [Figure 5].

229 **3.2.4 Strike and dip of the nominal plane** The first and second eigenvector rows of \mathbf{V} describe
 230 the planar fit in the absence of errors. The third eigenvector row of \mathbf{V} is orthogonal to the plane;
 231 this normal vector $\mathbf{n} = \mathbf{v}_3$ can be used with the mean of the dataset $\boldsymbol{\mu}_D$ (which the regressed
 232 plane passes through by definition), to form the plane equation

$$\mathbf{n} \cdot \mathbf{x} + \mathbf{n} \cdot \boldsymbol{\mu}_D = 0, \quad (8)$$

233 where \mathbf{x} is the set of all points that lie within the modeled plane. The nominal strike/dip in a
 234 geographic framework (*strike* defined relative to north) are calculated as follows:

$$(\text{strike}, \text{dip}) = \left(\tan^{-1} \frac{n_1}{n_2} - \frac{\pi}{2}, \cos^{-1} \frac{n_3}{\|\mathbf{n}\|} \right) \quad (9)$$

235 3.3 Confidence intervals for planar orientations

236 Errors to a planar measurements arise from statistical uncertainties on the parameters of a planar
 237 fit, and accurate modeling of errors requires the incorporation of a statistical distribution that is

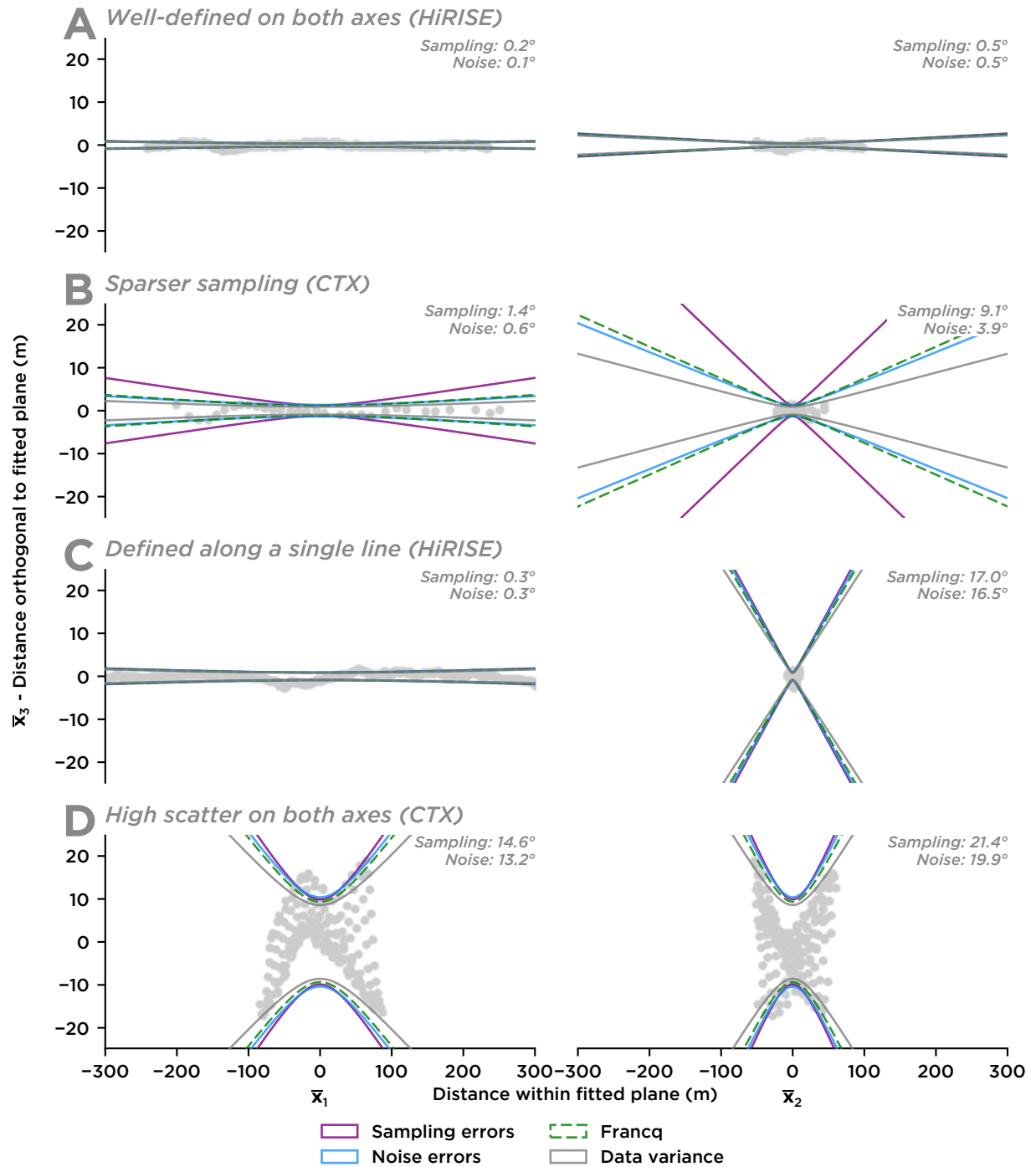


Figure 5: The Cartesian error space of fitted orientation measurements corresponding to example bedding traces [Figure 4]. Each plane is decomposed into two views aligned with \bar{x} , with in-plane variation shown on the horizontal axis and out-of-plane variation on the vertical. The data making up the planar measurement is shown as grey points, and hyperbolic error bounds computed by several methods are overlain. Angular errors are not to scale. Each fitted plane has a distinct error structure depending on the characteristics of the input point cloud. (a) A well-fitted plane with low errors on all axes. (b) A slightly poorer fit with minimal definition along \bar{x}_2 . (c) A plane well-defined along \bar{x}_1 but essentially undefined along \bar{x}_2 . (d) A fit poorly defined on both axes.

238 responsive to variation in input data quality. The PCA eigenvectors λ can be treated analogously
 239 to the OLS fit parameters $\hat{\beta}$ to define the error space to the plane, and the resulting orientation
 240 errors can be modeled by a hyperbolic shell with axes \mathbf{h} . Dataset-specific orientations errors are
 241 scaled by the Fisher (F) distribution to produce standardized statistical errors.

242 **3.3.1 Eigenvectors as regression parameters** The statistical basis for PCA regression errors can
 243 be developed from the widely-used OLS regression. The closed-form equation for OLS is given by

244

$$\hat{\beta}_{\text{OLS}} = (\mathbf{X}^T \mathbf{X})^{-1} \mathbf{X}^T \mathbf{y} \quad (10)$$

245 where \mathbf{X} is a matrix of explanatory variables ($n \times 2$ for planar fitting), \mathbf{y} is a column vector of n
 246 dependent measurements, and $\hat{\beta}$ is the two-element vector of regression coefficients. Regression
 247 errors are estimated using the variance of these fit coefficients,

$$\text{cov}(\hat{\beta}_{\text{OLS}}) = \sigma^2 (\mathbf{X}^T \mathbf{X})^{-1}, \quad (11)$$

248 where σ^2 is the scalar mean squared error of the residuals to the fit (*Fahrmeir et al.*, 2013, p. 117).

249 When rotated into $\bar{\mathbf{x}}$, the results of PCA transformation are directly comparable to OLS, al-
 250 lowing an expression for error to be adapted from standard statistical techniques. Errors are
 251 oriented along $\bar{\mathbf{x}}_3$ and conform by definition to the OLS assumption that errors are uniaxial,
 252 i.e. vertical only. Accordingly, $\hat{\beta}_{\text{PCA}} = [0, 0]$, since a fit plane expressed in $\bar{\mathbf{x}}$ has no slope. How-
 253 ever, $\text{cov}(\hat{\beta}_{\text{PCA}})$ is nonzero and can be used to construct errors analogous to those defined in
 254 OLS.

255 An expression for errors can be derived by recasting the PCA procedure into OLS notation.
 256 Recalling Equation 2, the covariance matrix \mathbf{C} of a mean-centered point cloud $\mathbf{M} = [\mathbf{X} \ \mathbf{y}]$ can be
 257 decomposed into subspaces:

$$\mathbf{C} = \frac{1}{n-1} \mathbf{M}^T \mathbf{M} = \frac{1}{n-1} \begin{bmatrix} \mathbf{X}^T \mathbf{X} & \mathbf{X}^T \mathbf{y} \\ \mathbf{y}^T \mathbf{X} & \mathbf{y}^T \mathbf{y} \end{bmatrix}_{3 \times 3}, \quad (12)$$

258 where n is the number of data points.

259 Transformed into $\bar{\mathbf{x}}$, this relationship reduces to $\mathbf{\Lambda} = \bar{\mathbf{C}} = \frac{1}{n-1} \bar{\mathbf{M}}^T \bar{\mathbf{M}}$. Since $\mathbf{\Lambda}$ is a diagonal
 260 matrix of eigenvalues,

$$\mathbf{X}^T \mathbf{X} = \text{diag}([\lambda_1, \lambda_2]) (n-1) \quad (13)$$

261 , $\mathbf{y}^T \mathbf{y} = \lambda_3 (n-1)$, and $\mathbf{X}^T \mathbf{y}$ and $\mathbf{y}^T \mathbf{x}$ contain only nullspace. Substitution for $\mathbf{X}^T \mathbf{X}$ in Equa-
 262 tion 11 yields

$$\text{cov}(\hat{\beta}_{\text{PCA}}) = \frac{\sigma^2}{n-1} \text{diag}([\lambda_1, \lambda_2])^{-1}. \quad (14)$$

263 Since the PCA eigenvalues are equivalent to the variance of the rotated data matrix along each

264 axis [Equation 7], we can further substitute $\sigma^2 = \lambda_3$. Since there are no covariances between the
 265 terms, the result reduces to

$$\text{var}(\hat{\beta}_{\text{PCA}}) = \frac{1}{n-1} \begin{bmatrix} \lambda_3 & \lambda_3 \\ \lambda_1 & \lambda_2 \end{bmatrix}, \quad (15)$$

266 a PCA regression error formulated in terms of eigenvectors.

267 **3.3.2 Errors limited by data variance** The statistical definition of the dataset centroid has im-
 268 portant implications for the structure of planar orientation errors, and we make a significant
 269 adjustment to this framework to account for the nature of the orientation-fitting problem. In
 270 standard regression statistics, the best-fitting plane is modeled to pass through the *mean* of the
 271 dataset, which is more precisely known as sample size increase, regardless of the variance of the
 272 dataset. The precision of the dataset mean is modeled by its variance, $\sigma_\mu^2 = \frac{\sigma^2}{n-1}$. This “mean-
 273 limited” construction is tailored to modeling potential correlations between variables and forms
 274 the basis for the regression errors derived in Equation 15.

275 For fitting geological planes, all data points should be treated as estimates of the *true value* of
 276 a single plane. The precision of the true value of the dataset is simply modeled by its variance,
 277 σ^2 . In this formulation of regression error, a high-quality fitted plane is defined by low variance,
 278 rather than well-known variance. This “variance-limited” framework explicitly models departures
 279 from a single plane, rather than the strength of correlations between scattered data.

280 Changing the definition of the dataset centroid substantially alters the error structure of the
 281 fitted plane. A mean-limited parametrization significantly overestimates angular certainty when
 282 sample sizes are large [Figure 6a], complicating comparisons of measurements with different sam-
 283 pling characteristics. In variance-limited statistics, the variance of data itself sets a floor for er-
 284 rors to the plane: large departures from an idealized plane are penalized and the basic structure of
 285 angular errors is preserved regardless of data density [Figure 6b]. This feature is crucial for com-
 286 paring planes with different sampling characteristics. Most “off-the-shelf” packages for planar
 287 fitting use standard mean-centered statistics, suggesting that measurements made using these
 288 packages may be fundamentally biased by sample size effects.

289 The mean-limited PCA regression errors expressed in Equation 15 can be adapted to the variance-
 290 limited framework by replacing the variance of the mean in Equation 14 with the variance of the
 291 dataset, which removes the $\frac{1}{n-1}$ scalar, yielding the simplified expression

$$\text{cov}(\hat{\beta}_{\text{PCA}}) = \sigma^2 \text{diag}([\lambda_1, \lambda_2])^{-1}. \quad (16)$$

292 This allows Equation 15 to be simplified to

$$\text{var}(\hat{\beta}_{\text{PCA}}) = \begin{bmatrix} \lambda_3 & \lambda_3 \\ \lambda_1 & \lambda_2 \end{bmatrix}. \quad (17)$$

293 The orientation error modeled by PCA regression is thus equivalent to the ratio of eigenvalues.

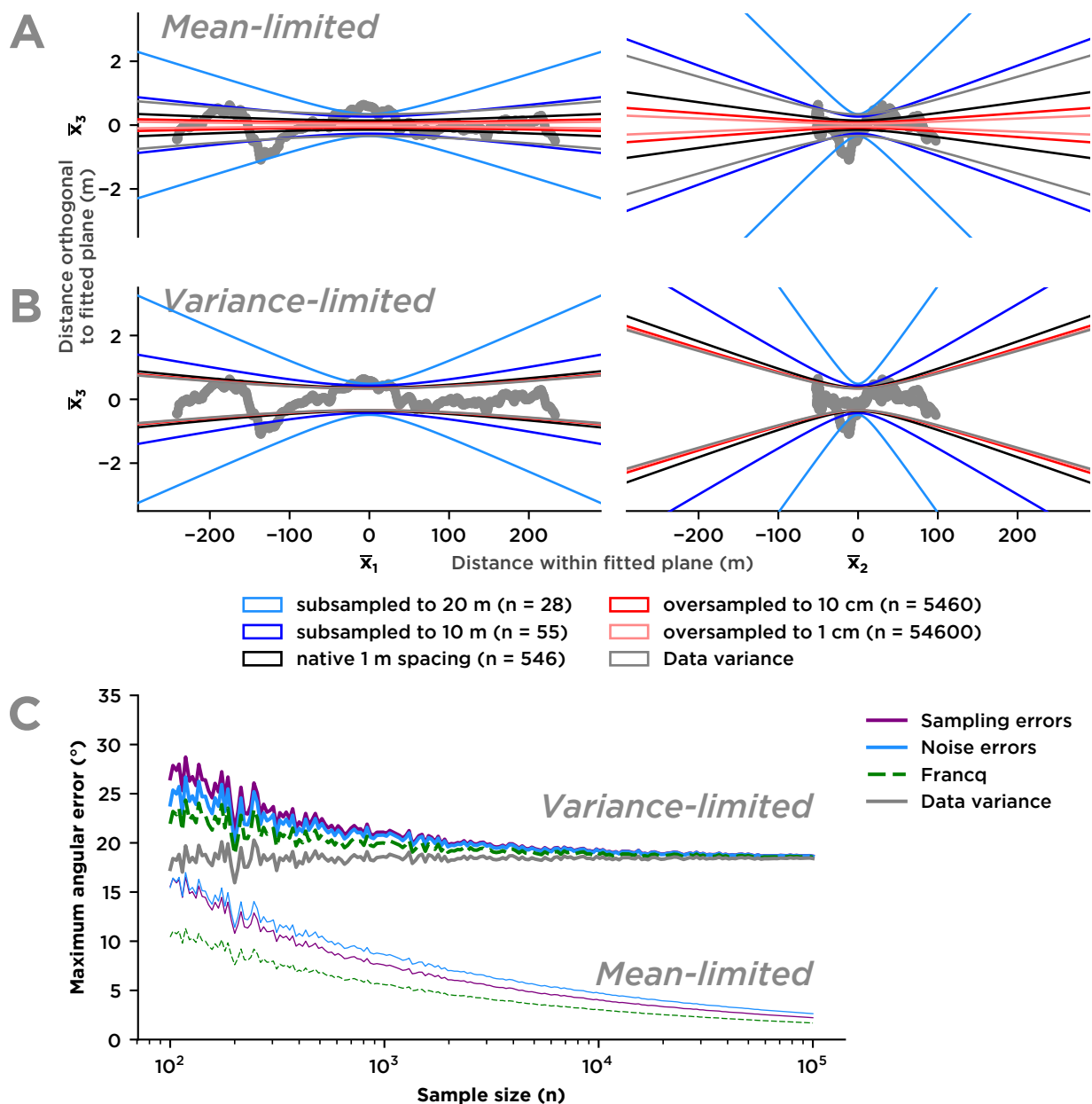


Figure 6: Exploration of centroid behavior with sample size. (a) Standard regression statistics applied to the “noise variance” method, with errors scaled to the quality of estimate of the mean. (b) Variance-limited regression modeling all points as estimates of a single true plane. This procedure is more resistant to dependence of error scaling on sample size. (c) Exploration of variance with sample size for a randomly generated plane with axial lengths $\mathbf{h} = [100, 10, 5]$, using several methods for variance estimation. All methods have errors that trend to 0 at large sample sizes when the dataset centroid is estimated by the mean.

294 **3.3.3 Population fit parameters** $\text{var } \hat{\beta}$ captures regression errors specific to the sample mea-
 295 sured and is a maximum-likelihood estimator of the error to the true population fit parameter,
 296 $\text{var } \beta$; that is, $\text{var } \beta = \text{var } \hat{\beta} + \text{error}(\text{var } \hat{\beta})$. $\text{var } \beta$ can be estimated using a statistical distribution
 297 that takes into account sample size and the degrees of freedom of the input data (e.g. *Fahrmeir*
 298 *et al.*, 2013).

299 For PCA, the eigenvalues λ_i that represent the dataset are equivalent to the sample variance
 300 of the dataset along each major axis [Equation 7], and the population variance along each axis
 301 is equivalent to $\lambda_i + \text{error}(\text{var } \lambda_i)$. Since PCA eigenvectors are orthogonal, their eigenvalues are
 302 statistically independent (*Jolliffe*, 2002, p. 46) and can be straightforwardly ratioed. Extending
 303 Equation 17, statistical errors to the planar estimator can be expressed as a ratio of uncertain
 304 eigenvalues:

$$\text{var } \beta_{\text{PCA}} = \left[\frac{\lambda_3 + \text{error}(\lambda_3)}{\lambda_1 + \text{error}(\lambda_1)} \quad \frac{\lambda_3 + \text{error}(\lambda_3)}{\lambda_2 + \text{error}(\lambda_2)} \right]. \quad (18)$$

305 The orthogonality of PCA allows regression errors to be represented as a symmetrical hyper-
 306 bolic surface [Figure 2] which can be manipulated with vector and tensor algebra, increasing flex-
 307 ibility for data visualization [Section 3.4]. The two orthogonal slopes that make up $\text{var } \beta_{\text{PCA}}$ are
 308 equivalent to tangents to an elliptic hyperboloid on two orthogonal axes. This error hyperboloid
 309 has semimajor axes defined by the vector expression $\mathbf{h} = \mathbf{p} \pm \mathbf{e}$, where \mathbf{p} represents the regression
 310 parameters and $\mathbf{e} = \text{error}(\boldsymbol{\lambda})$ represents the error to each eigenvalue. For mean-limited statis-
 311 tics, $\mathbf{p} = \left[\lambda_1, \lambda_2, \frac{\lambda_3}{n-1} \right]$, and for variance-limited statistics, $\mathbf{p} = \boldsymbol{\lambda}$. Thus, orientation uncertainty
 312 in the PCA framework can be represented as a hyperbola with eigenvalue axes:

$$\mathbf{h} = \boldsymbol{\lambda} \pm \mathbf{e}. \quad (19)$$

313 **3.3.4 Errors to eigenvectors** We extend our definition of \mathbf{e} to incorporate the Fisher statistical
 314 distribution, F :

$$\mathbf{e} = \text{error}(\boldsymbol{\lambda}) = F_{\alpha, d, n-d} \sigma_{\boldsymbol{\lambda}}. \quad (20)$$

315 $F_{\alpha, d, n-d}$ incorporates the number of samples in the dataset (n) the degrees of freedom of the
 316 statistical transformation (d), and the desired level of certainty (α). Typical values are $\alpha = 0.95$
 317 and $d = 2$ [see Section 3.3.5]. $\sigma_{\boldsymbol{\lambda}}$ is the standard error of the eigenvectors, which can be defined
 318 in several ways, as summarized below. Results for the four type cases are shown in Figure 5.

319 **Data variance** The most basic parametrization of orientation errors uses only variance of the
 320 input dataset (its eigenvalues, in PCA) to represent the error space without $\sigma_{\boldsymbol{\lambda}}$, resulting simply
 321 in $\mathbf{h} = \mathbf{p} = \boldsymbol{\lambda}$. The data variance defines the basic structure of the plane, including its scaling
 322 based on out-of plane residuals and the directional dependence of fit quality. However, without a
 323 statistical treatment of the accuracy of variance, this method is unresponsive to undersampling
 324 or differently-scaled datasets.

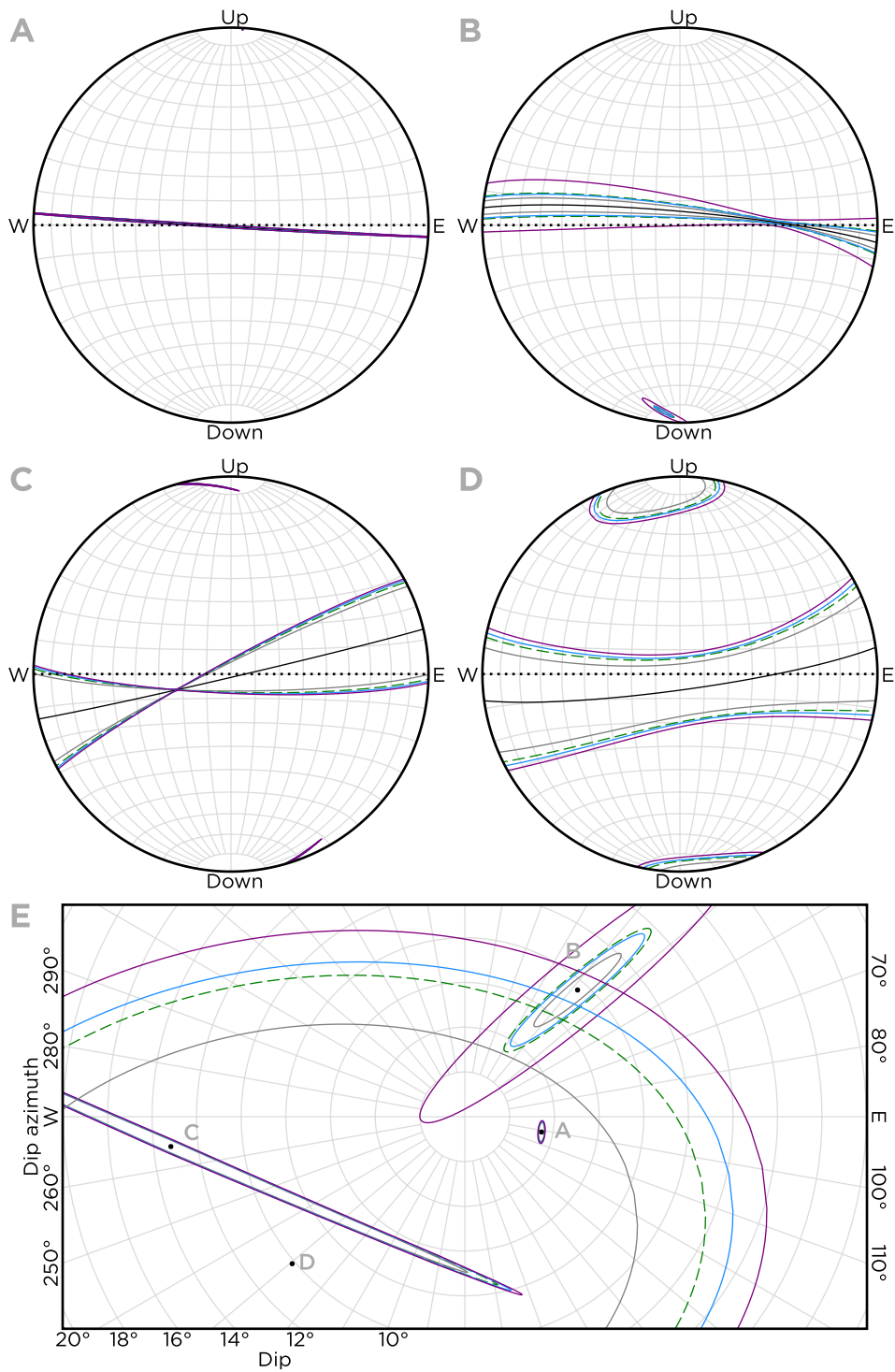


Figure 7: Projection of the hyperbolic errors to the plane into spherical coordinates to show angular errors. Estimates by different methods for computing \mathbf{h} are colored as in Figure 5. (a-d) Spherical error space for each of the planes shown in Figure 5, projected onto oblique upper-hemisphere, equal area stereonets. (e) Error space to the bedding pole for each of the planes in panels a-d.

325 The data variance parameterization of orientation errors is developed in the paleomagnetism
 326 literature, where uncertain lines and planes model magnetometer response during laboratory
 327 measurements of rock remnant magnetism (e.g. *Kirschvink*, 1980). This literature describes the
 328 parameterization of the PCA fit as an ellipsoid (the “dual” quadric to the hyperbola enclosing the
 329 plane; see Appendix A) with different potential shapes depending on dataset structure [Table 1,
 330 adapted from *Onstott* (1980)].

331 **Sampling variance** The simplest method of statistically-based error scaling uses multivariate
 332 statistics based on sample size. In this framework, errors assume that the measured data is a
 333 random sampling of a population that conforms to a Gaussian distribution. The expression for
 334 variance of the eigenvectors for PCA,

$$\sigma_{\lambda}^2 = \frac{2\lambda^2}{n-1}, \quad (21)$$

335 arises directly from the estimation of population variance in sampling statistics (*Jolliffe*, 2002,
 336 p. 48; *Faber et al.*, 1993).

337 **Noise variance** The standard assumption of Gaussian population statistics, that the variance
 338 of the sample is primarily a function of its size, may be imperfect when applied to continuously
 339 sampled data. Datasets that include all of the available data over an interval (i.e. are not random
 340 samples of a population) are implicitly highly correlated, so sample-size based statistics may be
 341 misleading. Interpolated elevation data can easily be smoothed and overfitted, increasing appar-
 342 ent statistical power with little to no improvement in the quality of the fit. Conversely, when the
 343 noise in the input dataset is low, even small samples can show significant results. The noise vari-
 344 ance framework for PCA errors (*Malinowski*, 1977; *Faber et al.*, 1993, 1995; *Faber and Kowalski*,
 345 1997) is explicitly designed for use with continuously sampled data.

346 Instead of uniformly scaling errors along a given principal component axis \bar{x}_i , noise covari-
 347 ance is based on the intuition that “measurement noise” defined along higher-dimensional axes
 348 provides a good estimate of the errors on all axes. In our case, scatter along \bar{x}_3 is the “noise
 349 component” of the data, and may provide a better estimate of the scatter in \bar{x}_1 and \bar{x}_2 than the
 350 variance along these axes. Intuitively, the structure of the data cloud within the best-fitting plane
 351 represents “signal” and its structure should not be used as a measure of error.

352 *Faber et al.* (1993) shows that the variance of the PCA eigenvectors can be modeled as

$$\sigma_{\lambda}^2 = 4 \lambda \sigma_{\hat{M}}^2, \quad (22)$$

353 where $\sigma_{\hat{M}}^2$ is the “noise variance” of the data matrix. Methods to compute the noise variance $\sigma_{\hat{M}}^2$
 354 rely on the concept of “pseudorank”, the rank of the aligned data matrix in the absence of noise.
 355 Detailed treatments of the noise variance framework (*Faber et al.*, 1995; *Faber and Kowalski*, 1997)

356 discuss adjustment of the pseudorank to incorporate nonlinear bias, but this is unnecessary for
 357 our low-dimensional case. For three-dimensional data aligned along a plane, errors will be entirely
 358 contained in scatter on \bar{x}_3 . A plane without noise will be contained in the \bar{x}_1 - \bar{x}_2 plane, with a
 359 pseudorank of $K = 2$.

360 *Malinowski (1977)* describes the “real error” component

$$\sigma_{\hat{\mathbf{M}}}^2 = \frac{\sum_{p=K+1}^c \lambda_p}{r(c-K)} \quad (23)$$

361 where $r \times c$ is the dimensions of the data matrix \mathbf{M} . *Faber et al. (1993)* slightly modifies this to

$$\sigma_{\hat{\mathbf{M}}}^2 = \frac{\sum_{p=K+1}^c \lambda_p}{(r-K)(c-K)} \quad (24)$$

362 based on experimental validation. For our purposes of planar fitting, $K = 2$, $r = n$, and $c = 3$,
 363 and these expressions collapse to $\sigma_{\hat{\mathbf{M}}}^2 = \frac{\lambda_3}{n}$ (*Malinowski, 1977*) and $\sigma_{\hat{\mathbf{M}}}^2 = \frac{\lambda_3}{n-2}$ (*Faber et al., 1993*).
 364 With sample sizes $n \gg K$, the difference between these estimators is negligible. Combining
 365 Equation 22 with Equation 24, we can express the noise variance of the dataset as

$$\sigma_{\lambda}^2 = \frac{4\lambda\lambda_3}{n-2}. \quad (25)$$

366 **Other statistical distributions** Several other treatments of errors given in the literature pro-
 367 vide direct alternatives for scaling \mathbf{e} with different statistical assumptions. *Franco and Govaerts*
 368 (2014) provides a formulation of error bars for two-axis OLS, which can be generalized to the PCA
 369 framework, yielding error axes

$$\mathbf{e} = \lambda \sqrt{\frac{2}{n-2}} F_{\alpha, d, n-d}. \quad (26)$$

370 This formulation provides slightly more constrained errors than both sampling and noise-based
 371 errors, due to the co-dependence of errors of variables defined in global Cartesian coordinates.
 372 *Babamoradi et al. (2013)* provides an implementation that closely tracks the “sampling variance”
 373 method with slightly different scaling for sample sizes. *Weingarten et al. (2004)* describes a nu-
 374 merical method which applies OLS regression after PCA rotation, using the slope found by OLS
 375 in $\bar{\mathbf{x}}$ to estimate $\text{var } \beta_{\text{PCA}}$.

376 **Preferred choice of σ_{λ} (or \mathbf{e})** The effect of using different test statistics is minimal for well-
 377 sampled data, and results asymptotically converge on the data variance at large sample sizes [Fig-
 378 ure 5 and 7]. The formulations tested show similar results, but the “noise variance” is more re-

379 sistant to changes in sample density [Figure 5c and d]. We use the noise error as the preferred
 380 scaling in software and graphical implementations of this method.

381 **3.3.5 Statistical error scaling** To create confidence intervals, we apply the Fisher ($F_{\alpha,d,n-d}$) sta-
 382 tistical distribution and the formulation of σ_{λ} from Equation 25. to Equation 20. The eigenvalues
 383 of the dataset each follow the $\chi^2_{\alpha,d}$ distribution. The Fisher distribution, $F_{\alpha,d,n-d}$, which models
 384 ratios of χ^2 -distributed parameters (Jolliffe, 2002; Francq and Govaerts, 2014; Babamoradi et al.,
 385 2013), is the appropriate test statistic for orientation data, since regression parameters are com-
 386 posed of ratios of eigenvalues [Equation 17]. At large sample sizes, $\lim_{n \rightarrow \infty} F_{\alpha,d,n-d} = \frac{1}{d} \chi^2_{\alpha,d}$.

387 For planar orientations, $d = 2$, since the orientation information contained in the three
 388 eigenvectors can be summarized as two ratios. The remaining parameter, α , is the confidence
 389 level at which the distribution should be queried. For typical analysis, $\alpha = 0.95$, corresponding
 390 to a 95% confidence interval, should suffice.

391 The resulting parameterization of the errors to the eigenvectors is summarized for noise er-
 392 rors as

$$\mathbf{e}_{\lambda} = F_{\alpha,d,n-d} \boldsymbol{\sigma}_{\lambda} = F_{\alpha,d,n-d} \sqrt{\frac{2\lambda}{n-2}} \lambda_3. \quad (27)$$

393 To construct the hyperbolic error space of the plane, we recall that $\mathbf{h} = \boldsymbol{\lambda} \pm \mathbf{e}$ [Equation 19]. At
 394 any level of error, the maximum bounding surface of \mathbf{h} occurs when the length of in-plane axes
 395 of the hyperboloid are minimized and out-of-plane error is maximized. Thus, the maximum error
 396 shell used for visualization is

$$\mathbf{h}_* = [\lambda_1 - e_1, \lambda_2 - e_2, \lambda_1 + e_3], \quad (28)$$

397 or alternatively

$$\mathbf{h} = \boldsymbol{\lambda} + \mathbf{a} F_{\alpha,d,n-d} \boldsymbol{\sigma}_{\lambda}, \quad (29)$$

398 where $\mathbf{a} = [-1, -1, 1]$ controls the direction along which errors are applied to form the maximum
 399 error surface.

400 3.4 Displaying orientation error surfaces

401 Projections of error bounds as 2D hyperbolic slices, spherical ellipses, and girdles provide useful
 402 visualizations of the error structure of the plane, relying only on the statistically derived hyper-
 403 boloid with semiaxes \mathbf{h} [Figure 2]. This represents the uncertain plane (independent of the sta-
 404 tistical assumptions used in its construction). Generalized equations for quadric surfaces that
 405 can be manipulated with transformation matrices and quaternion rotations are discussed in Ap-
 406 pendix A; here we focus on common cases used to develop key visualizations of the error space.

407 **3.4.1 Projection to hyperbolic errors** Two-dimensional conic slices of the hyperbolic error space
 408 of the plane summarize dataset structure, both in PCA-aligned and global coordinates. Errors can

409 be assessed along any axis, but slices of the error hyperboloid aligned with the major axes of the
 410 planar fit are the most intuitive. These “axis-aligned” views of the dataset, with in-plane variation
 411 on the horizontal axis and out-of-plane variation on the vertical, are the ideal decomposition to
 412 assess the structure of a fitted dataset and verify the quality of the input data \mathbf{D} . Visual inspection
 413 of dataset quality in PCA-aligned coordinates [Figure 5] is an important quality check on
 414 measured orientations. Several measurements [Figure 5b and d] show significant out-of-plane
 415 variation potentially related to both DEM errors and digitizing errors.

416 A hyperbola can be constructed for a two-dimensional slice of the error quadric, along a coordinate
 417 basis $\bar{\mathbf{x}}_\gamma = [\bar{x}_\gamma, \bar{x}_3]$ with axis \bar{x}_γ within the plane defined as

$$\bar{x}_\gamma = \sqrt{\bar{x}_1 \cos^2 \gamma + \bar{x}_2 \sin^2 \gamma}, \quad (30)$$

418 a linear combination of \bar{x}_1 and \bar{x}_2 where $\gamma = [0, 2\pi]$ is the angle from \bar{x}_1 within the plane. Accordingly,
 419 h_γ can be defined as an axis of the 3D conic intermediate between h_1 and h_2 (and a
 420 major axis of its 2D projection),

$$h_\gamma = \sqrt{h_1 \cos^2 \gamma + h_2 \sin^2 \gamma}. \quad (31)$$

421 The 2D hyperbolic slice of the error quadric aligned with axis \bar{x}_γ can be represented as

$$\mathbf{C}_H = \text{diag} \left(\frac{1}{h_\gamma^2}, -\frac{1}{h_3^2}, 1 \right). \quad (32)$$

422 For a slice of the plane oriented along \bar{x}_1 , $\gamma = 0$ and $\mathbf{h}_\gamma = [h_1, h_3]$. For an axis-aligned and
 423 mean-centered conic, the hyperbolic error bounds in are given by the equivalent representations
 424

$$\bar{x}_3 = \pm h_3 \cosh \left(\sinh^{-1} \left(\frac{\bar{x}_\gamma}{h_\gamma} \right) \right) = \pm h_3 \sqrt{\left(\frac{\bar{x}_\gamma}{h_\gamma} \right)^2 + 1}. \quad (33)$$

425 These error bars can be plotted as-is (e.g. Figure 5) or shifted from \bar{x}_γ to \mathbf{x} using scaling and
 426 rotation as necessary. We discuss this more general transformation in Appendix A.

427 **3.4.2 Spherical representation of errors** The discussion and display of orientation errors has
 428 thus far been carried out in a Cartesian reference frame, but it is useful to represent uncertain
 429 planar fits in an angular framework. This allows plotting on stereonet and direct comparison to
 430 other orientation data.

431 For our rotational construction, given any in-plane axis h_γ , the angular errors from the non-
 432 inial plane are defined by tangents to the hyperbolic error sheets,

$$\theta_\gamma = 2 \tan^{-1} (h_3/h_\gamma), \quad (34)$$

433 the factor of 2 arising from combining errors for both the upper and lower sheets of the hyper-
 434 boloid. Solving this for $\gamma = [0, 2\pi]$ yields a girdle of angular error magnitudes relative to the
 435 great circle defining the nominal plane. The resulting distribution is a graphical representation
 436 of angular errors for all directions of the planar fit [Figure 7].

437 The angular error surfaces for the normal vector fall 90° from those representing the plane,
 438 forming an elliptical error space that encompasses poles to the plane. Normal vector errors can
 439 be computed by a similar process to that used to generate a hyperbolic girdle around the
 440 plane, using the inverse of the tangents.

$$a_\gamma = \tan^{-1} (h_\gamma/h_3) \quad (35)$$

441 evaluated over $\gamma = [0, 2\pi]$ defines the angular dimension of an error ellipse in spherical coordi-
 442 nates, defined relative to \bar{x}_3 . This ellipse can be rotated into global coordinates using the rotation
 443 matrix \mathbf{V} . A more general solution is discussed in Appendix A.2.

444 **3.4.3 Maximum and minimum angular errors** The best numerical summary of errors to an ori-
 445 entation measurement are the maximum and minimum angular errors, which are defined orthog-
 446 onal to the plane and aligned with the major axes of the best-fitting plane. This concept can also
 447 be applied to statistically derived error surfaces, given a set of axial lengths calculated by one of
 448 the methods above. For the semiaxes \mathbf{h} corresponding to errors at a particular level,

$$(\theta_{\max}, \theta_{\min}) = (2 \tan^{-1} (h_3/h_2), 2 \tan^{-1} (h_3/h_1)) \quad (36)$$

449 provides the angular width of the error distribution aligned with the major axes of the dataset.
 450 This allows errors to be reported in angular space, though their statistical development is under-
 451 taken entirely in Cartesian space. Because of the nonlinearity associated with angular transfor-
 452 mations, there is no natural correspondence between the dip direction of a best-fitting plane and
 453 the direction of θ_{\max} . To form a full representation of the errors, we must also report the azimuth
 454 of the error axis within the plane. This *rake* angle [Table 2] is defined as the angle between the
 455 strike and θ_{\max} (which is oriented along \bar{x}_2), calculated as

$$rake = \cos^{-1} ((\mathbf{v}_3 \times \mathbf{z}) \cdot \mathbf{v}_2), \quad (37)$$

456 where $\mathbf{z} = [0, 0, 1]$ is a vertical vector.

457 3.5 Joint fitting of parallel bedding planes

458 A common problem for remote sensing of geologically relevant areas is lack of continuous ex-
 459 posure, and planes that are unconstrained in one dimension are common [Figure 4]. However,
 460 exposures of bedding in close spatial association often capture slightly different cuts of topogra-

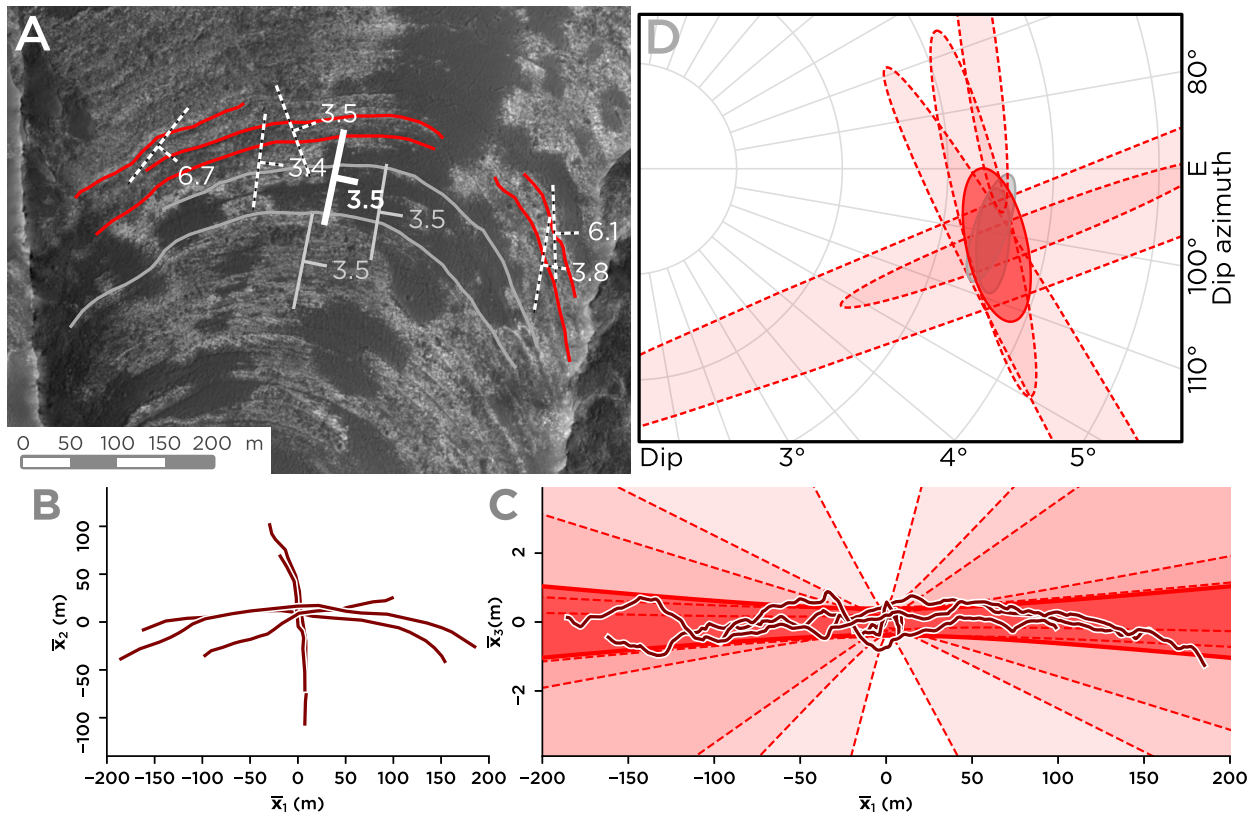


Figure 8: Joint fitting of bedding traces within a single stratigraphy to minimize errors for parallel planes. (a) Map view of bedding traces showing scattered nominal dips for bedding traces on opposing hillslopes (dashed), along with better-constrained orientations digitized around the entire range of hillslope aspect (solid bold). (b) Plan view of bedding traces centered and stacked atop each other for joint fitting, showing definition of a plane in two dimensions. (c) Side view of the plane showing residuals within the digitized dataset. Jagged lines are due to digitization errors. (d) Projection of errors to bedding poles on an upper-hemisphere stereonet, showing the grouped error range (red filled) at the intersection of the individual error spaces (dashed), and overlapping the error spaces of well-digitized single planes.

461 phy with different orientation error structures. This is statistically useful: under the assumption
462 of parallel bedding, multiple bedding traces can be jointly fitted to increase the three-dimensional
463 definition of a planar dataset. Error metrics computed after fitting can be used to test the validity
464 of this assumption.

465 In Figure 8, several bedding traces digitized on opposing hillslopes in the same cuesta show
466 different error structures. Bedding traces that could be followed around the entire range of hill-
467 slope aspect have much more restricted error spaces. Grouping of the low-quality planar fits cre-
468 ates a much higher-precision joint measurement at the intersection of the error spaces of indi-
469 vidual beds, showing nearly the same orientation as high-precision single-bed measurements.

470 The process of joint fitting is nearly the same as the single-plane fitting procedure outlined in
471 Section 3.2 and 3.3. The only difference is in processing of the input data: prior to PCA regres-
472 sion, the data matrix \mathbf{D} corresponding to each input point cloud is independently centered on its
473 mean using Equation 1. The resulting matrices are stacked to form a single centered data matrix
474 \mathbf{M} . This combined representation contains orientation info for each bedding trace but discards
475 information on the relative locations of the planes. The orientation of the combined data matrix
476 is regressed using PCA and error is modeled using standard techniques. If the assumption of a
477 shared bedding orientation is valid, this can vastly increase statistical power.

478 This technique removes the need for certainty in the bed-to-bed correspondence of adjacent
479 but discontinuous stratigraphic exposures, which is often difficult to determine. However, the
480 method must be applied with care: it is only valid where the assumption of parallel bedding holds.
481 For this reason, the combination of this method with views of decomposed variance and statisti-
482 cal error bounds is particularly powerful. Evaluation of misfits from the joint plane can illuminate
483 whether the assumption of shared stratigraphy is valid. If a grouping cannot be adequately mod-
484 eled as a parallel stratigraphy, this will be clear from the input data. Joint fitting of planes can
485 be valuable both for precise statistical modeling of parallel-bedded stratigraphies and as an ex-
486 ploratory tool to evaluate whether stratigraphies conform to a parallel-bedding assumption.

487 **4 Method demonstration and performance**

488 **4.1 Orbital imagery of the San Rafael Swell, Utah**

489 The San Rafael Swell in eastern Utah, USA, is a $\sim 20 \times 40$ km Paleocene Laramide anticline formed
490 above a west-dipping thrust fault in the subsurface that tilted the strata to nearly vertical, creating
491 the imposing San Rafael “Reef” [Figure 9a]. This structure is cored by a Jurassic stratigraphy
492 including the distinctive, thick aeolian Navajo sandstone (*Gilluly and Reeside Jr, 1928*). In the
493 middle of the swell, these strata are eroded away. The dramatic transect of Interstate 70 across
494 the center of the structure makes the San Rafael Swell a world-famous structural locale. At the
495 eastern edge of the swell, eastward dips steepen from near-flat to a maximum of $\sim 60^\circ$ before
496 shallowing outside of the reef [Figure 9b]. The simple fold pattern and well-exposed stratigraphic

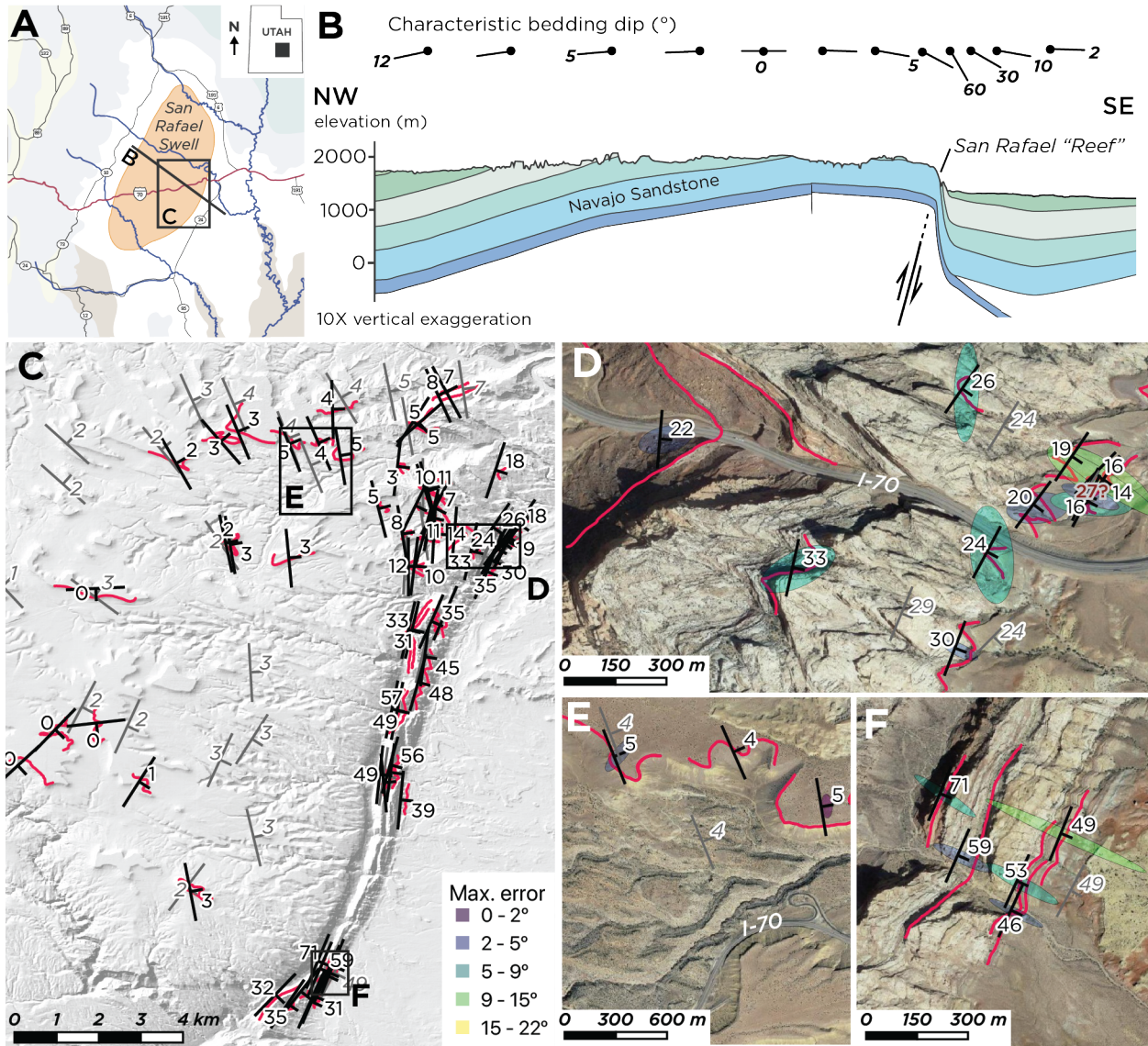


Figure 9: (a) Physiographic context of the San Rafael Swell in southeast Utah, USA. (b) Cross-section of the San Rafael Swell anticline (after *Doelling et al.*, 2017) showing the asymmetric dips of strata across the structure. (c) Field-measured bedding orientations (grey numbered symbols) from the San Rafael Desert geologic map (*Doelling et al.*, 2017), nominal remotely-sensed bedding orientations (black numbered symbols), and corresponding digitized bedding traces (red lines) atop a hillshade of the 5m aerial photogrammetric DEM used as input data for orientation reconstruction. Field-measured and remotely-sensed bedding orientations follow the same structural pattern. (d-f) Digitized bedding traces, remotely-measured orientations and field orientations atop orthorectified, coregistered *Google Maps* satellite data (accessed Feb. 2018) for key areas. Remotely-sensed orientations are underlain by an error-ellipse with axial lengths corresponding to θ_{\max} and θ_{\min} , oriented along the maximum direction of error.

497 layering provide an ideal setting to test the recovery of orientation errors from orbital or airborne
498 data, allowing orientation recovery to be tested at a wide range of dips against data collected *in-*
499 *situ*.

500 **4.1.1 Datasets** The map database accompanying the recently published geologic map of the San
501 Rafael Desert (*Doelling et al.*, 2017) provides bedding orientations from the structural map, which
502 were measured in the field at outcrop scale using a compass clinometer. At regional scale, they
503 outline the convex structure and N-S axis of the swell [Figure 9c]

504 A 5 m ground-sample-distance DEM from the Utah Automated Geographic Reference Center
505 was used as the elevation layer for digitized bedding traces. This DEM was created from autocorre-
506 lated 1-meter resolution stereo aerial imagery, using the SOCET Set software package. Elevation
507 contours and a shaded-relief map were generated from the DEM to inspect alignment and data
508 fidelity. In general, the DEM is of high quality, with a few artifacts in high-slope regions on the
509 eastern side of steep hillsides where shadows lead to poor correlations. Locally, the data is sig-
510 nificantly higher fidelity than the 10-meter resolution National Elevation Dataset (*Gesch et al.*,
511 2014)

512 Orthorectified, mosaicked ~25 cm/px satellite imagery from Google Maps was used to digitize
513 bedding traces atop the DEM. The satellite imagery had been warped over a somewhat lower-
514 resolution DEM than used here, leading to registration errors of up to 5 meters between the DEM
515 and imagery datasets. Areas with obvious mismatch were avoided for digitization of features.

516 Bedding traces were digitized atop the satellite imagery using QGIS. Outcrops were chosen to
517 maximize the 3D structure of captured planes, and areas near field-measured observations were
518 targeted for direct comparison. Lengths of bedding traces range from 100 to 2500 m (median
519 length 415 m). The longest traces are in low-dipping strata in the western portion of the study
520 area. Digitized bedding traces are shown in Figure 9c.

521 The orienteer software package (see Appendix) was used to conduct planar fitting and eval-
522 uate the resulting planes for quality. During elevation extraction, lines were subset at 5 meter
523 intervals to fully query the DEM. Planes were examined visually and quantitatively after PCA fits
524 as described above. Those with large residuals (typically > 10 m out-of-plane) were re-measured
525 if the blunder was due to obvious mis-digitization, or discarded [Figure 10]. Sixty-eight planes
526 were retained. Since only planes with favorable exposure were measured, no grouping of beds
527 was required to increase statistical power.

528 **4.1.2 Orbital and field data comparison** Overall, the map pattern of remotely-measured orien-
529 tations mimics the large-scale structural trend of steepening dips towards the eastern monocline
530 of the swell [Figure 9c]. Dip magnitudes are very close to those measured in the field. The direc-
531 tion and magnitude of errors are summarized as ellipses on the dip symbols. For the shallowest
532 bedding, errors are extremely low [Figure 9d], while for the steepest measurements, errors are
533 almost entirely in the dip direction [Figure 9e]. Error magnitudes are small for low-dipping strata

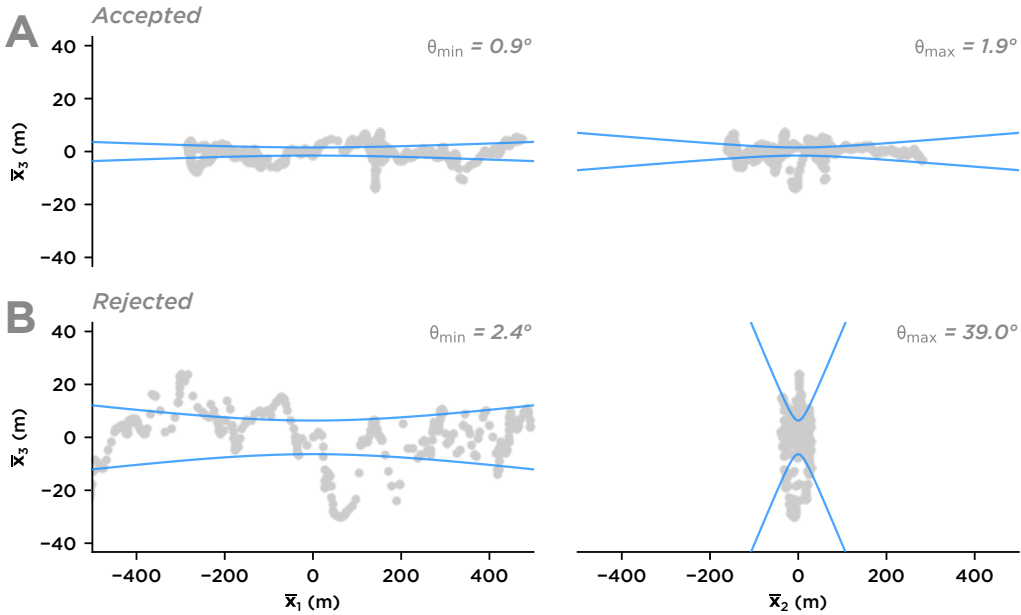


Figure 10: Axis-aligned visualization of fit errors to illustrate filtering criteria for poor bedding traces during creation of the San Rafael Swell dataset. **(a)** An accepted fit with relatively low out-of-plane scatter, defined over a significant length along both \bar{x}_1 and \bar{x}_2 . **(b)** A poor fit, with higher out-of-plane scatter and no definition along \bar{x}_2 . This bedding trace was discarded from the dataset.

534 and increase substantially with steeper dips. This is intuitive as the effects of DEM errors, poor
 535 registration of imagery, and digitizing errors will increase in rugged topography.

536 Selected closely spaced in-situ and remotely sensed orientation measurements paired for direct
 537 comparison [Figure 11] show that remotely-sensed orientations typically closely match the
 538 in-situ measurements, typically within error. Mismatch of a few degrees, especially in strike, can
 539 be explained by actual localized variation in bed orientation or slight measurement errors either
 540 in remote or in-situ gathered data. One measurement, highlighted in red on Figure 11, has an un-
 541 usually large mismatch with in-situ data. This measurement, at the eastern margin of the swell
 542 immediately north of the I-70 freeway, has a reported dip of 27° . We instead measure a dip, with
 543 error, of $10\text{-}20^\circ$ and replicate this result with additional measurements of several closely spaced
 544 beds. The 27° dip is steeper than those immediately to the west, putting it at odds with the local-
 545 ized structural pattern of shallowing dips at the eastern edge of the swell. This suggests that the
 546 published dip measurement for this outcrop may be in error.

547 Although basic correspondence between the DEM and imagery was manually checked, no process-
 548 ing or alignment was applied to the input data. A higher level of processing might increase the
 549 fidelity of the digital surface model, but this example demonstrates that reasonable planar orien-
 550 tations can be extracted from minimally-processed, publicly available imagery datasets, especially
 551 when good exposure is available. The addition of error and its visualization to the analytical prod-
 552 uct enables much more flexibility in input data quality, as errors arising from poorly registered

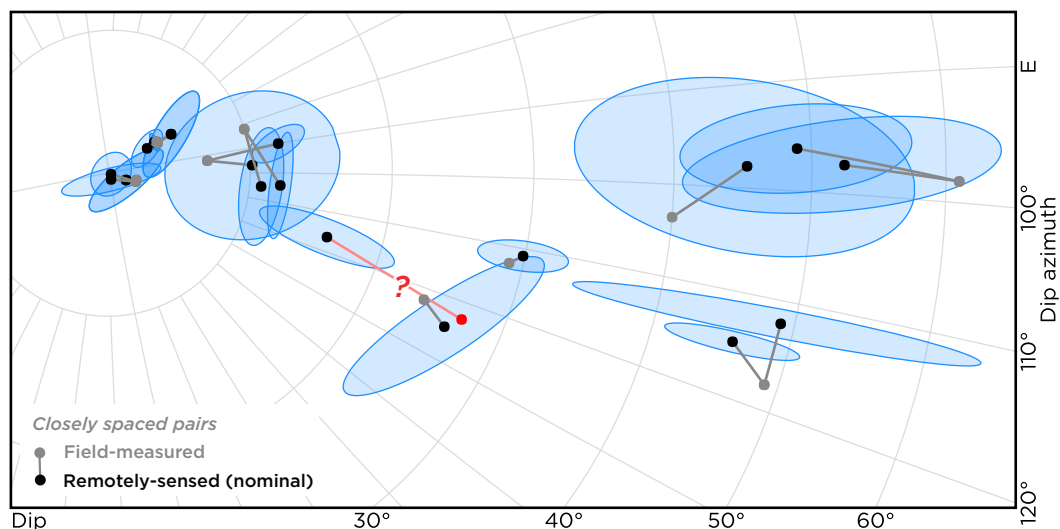


Figure 11: Upper-hemisphere stereonet showing poles to bedding for pairs of closely spaced field- and remotely-measured bedding orientations in the San Rafael Swell [Figure 9]. Errors generally increase at steeper dips (towards the right). One literature measurement (highlighted with a red ? and corresponding to the same symbol in Figure 9d) is steeper than all nearby remotely-sensed dips and does not conform to the regional structural pattern, suggesting that it may be an error in the preparation of the geologic map.

553 data or sloppy digitizing will be penalized by poor confidence metrics and readily recognized [e.g.
 554 Figure 10].

555 **4.2 UAV photogrammetry in the Naukluft Mountains, Namibia**

556 The eastern face of the Naukluft mountains adjacent to Onis Farm (24.32° S, 16.23° E) contains
 557 mixed siliciclastic and carbonate strata above a regionally significant thrust fault (*Rowe et al.*,
 558 2012). Recent mapping and stratigraphic studies in the area identified a minimally deformed
 559 stratigraphic section of the Zebra Nappe above this basal thrust fault (*Quinn and Grotzinger*,
 560 2016). Using UAV imagery gathered during this field study [Figure 12a], we construct a coarse-
 561 resolution digital outcrop model of this area [Figure 12a]; this dataset is used to test the recovery
 562 of bedding orientations by the techniques described in this paper. Assessing the quality of mea-
 563 surements by UAVs is of significant interest for terrestrial field geological studies (e.g. *Cawood*
 564 *et al.*, 2017), and multi-view aerial data tests the functionality of the method with off-vertical
 565 errors and ad-hoc photogrammetry that characterize UAV-based surface model creation.

566 **4.2.1 Datasets** An 80-m elevation range within the ~300 m cliff face at Onis Farm was cho-
 567 sen for this comparison, comprising the upper Ubisis Formation, the Tsams Formation, and the
 568 lower Lemoenputs Formation of the Zebra Nappe; field structural data was subset from a strati-
 569 graphic dataset assembled for the entire cliff (*Quinn and Grotzinger*, 2016). Within the target
 570 elevation range, bedding orientation measurements were collected at six locations with a Brun-
 571 ton compass clinometer, and the GPS position and description of the measured bed were logged
 572 [Figure 12]. The elevation of each measurement was determined after measurement by draping

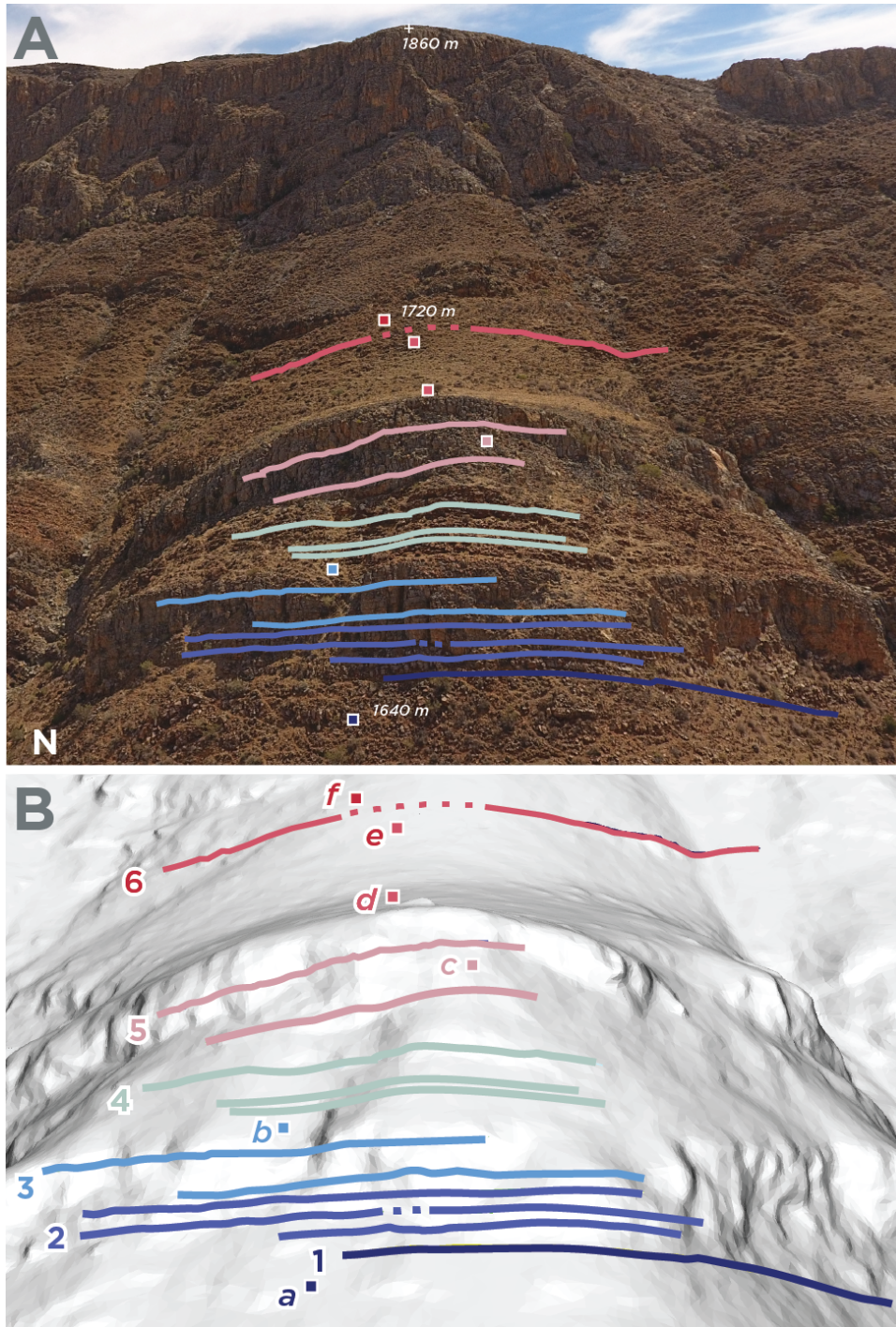


Figure 12: (a) UAV photograph (~500 m standoff) looking NW towards the cliffs at Onis Farm, Naukluft Mountains, Namibia. Digitized bedding traces (colored lines) and the locations of field-measured orientations (colored squares) are superposed. Beds dip ~30-45° degrees into the hillslope (away from viewer). 230 m of topographic relief is shown in the photo. (b) Digital surface model from UAV photogrammetry, viewed from slightly below the viewpoint of panel a, with digitized bedding traces superposed. Bedding traces grouped for analysis are connected by dashed lines. Groups of bedding traces with similar properties are numbered 1-6; field-measured orientations are lettered a-f.

573 the georeferenced data atop an Advanced Land Observing Satellite (ALOS) global 15-m resolution
574 photogrammetric DEM, which was used as a regional topographic basemap.

575 Outcrop images were acquired using a remotely piloted DJI Phantom 4 quadcopter UAV, from
576 an altitude of ~200 m above ground and ~500-800 m lateral standoff southeast of the target cliff.
577 The aircraft was approximately level with the target stratigraphic interval [Figure 12a]. UAV im-
578 ages were combined into a photogrammetric 3D model using the Agisoft Photoscan Professional
579 v1.2 structure-from-motion software package [Figure 12b]. The 3D model extends ~1.5 km later-
580 ally along the cliff face and captures ~400 m of relief on the east-facing cliff; it was assembled with
581 the “very high” quality setting and has ~4 million constituent points and a horizontal resolution
582 of ~15 cm per pixel. In all dimensions, model precision varies within the scene depending on the
583 stereo convergence geometry of individual image pairs.

584 The stratigraphic interval studied contains two cliff faces with intervening float-covered slopes;
585 beds traceable in UAV imagery primarily occur on the cliffs. The traces of 14 bedding surfaces
586 were digitized manually in Agisoft Photoscan atop oblique images registered to the 3D model
587 [Figure 12]. Agisoft Photoscan automatically drapes digitized bedding traces onto the surface
588 model, creating a 3D point dataset without an additional software package or conversion to a
589 gridded DEM. Digitized bedding traces were exported as a dxf-format file using the UTM Zone
590 33S coordinate system. The `fiona` Python module was used to read this data, and the `attitude`
591 software package was used for planar fitting. Four bedding traces were grouped with other traces
592 at similar stratigraphic levels to increase statistical power, yielding a final set of 12 distinct orien-
593 tation measurements. An `iPython` notebook containing the analytical pipeline for this example
594 is available as supplementary material to this publication.

595 **4.2.2 UAV and field data comparison** Field-measured bedding orientations for the target strati-
596 graphic interval range in strike from 225-245°, corresponding to dip azimuths of 315-335°. Dips
597 range from 30 to 45° to the northwest (into the hillslope). Field-measured orientations are let-
598 tered *a-f*, and sets of remotely-sensed measurements are numbered 1-6 [Figure 12b and 13].

599 The lowest-elevation extracted bedding trace (1) follows a coarse sandstone bed across the
600 nose of the hillslope. Its orientation is well-constrained, with a maximum angular error of ~5°,
601 but significantly different from the field-measured orientation of a siltstone bed ~10 m strati-
602 graphically below (*a*). This mismatch may result from an actual dip change due to slight folding
603 across the lithologic boundary at the base of the cliff.

604 The next intervals (2 and 3) contain five beds within a cliff-forming dolomite unit; two of
605 these measurements were grouped. The beds in 2 and 3 have error ellipses elongated in the dip
606 direction, representing measurements well-constrained on a single axis (roughly, their apparent
607 dip in standoff imagery); their error spaces overlap that of (1), suggesting consistent bedding
608 orientations for the entire lower cliff.

609 Beds marked as 4 occur in a fine-medium sandstone interval where staircase beds are easily

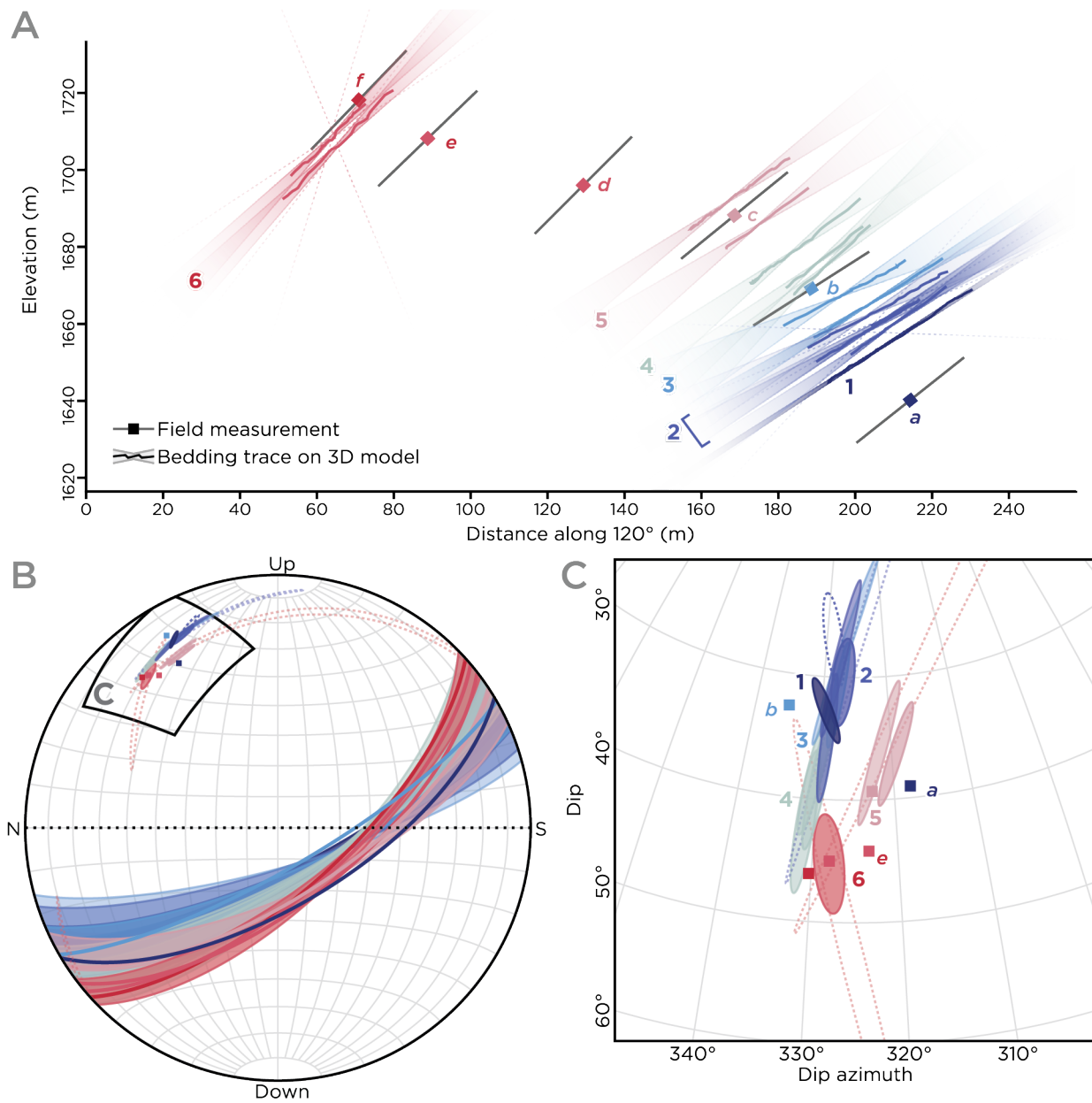


Figure 13: Comparison of field-measured and UAV photogrammetric bedding orientations for the Onis cliffs. Remotely-sensed and field-measured bedding orientations are colorized by height. In each panel, error spaces for individual remotely-sensed measurements are shown as colored fields. Dotted lines show the error bounds of measurements prior to grouping. (a) Orthographic projection of bedding orientations, with the horizontal axis showing distance to the southeast, approximately along the dip direction measured beds. Remotely-measured beds are shown as residuals to their best-fitting plane and overlain by hyperbolic error bounds. The recovery of dips into the hillslope by remotely-sensed orientations is apparent. (b) Upper-hemisphere oblique equal-area stereonet showing NW-dipping bedding girdles for remotely-sensed and field measurements. Dotted lines represent the edges of error ellipses for components of grouped measurements. (c) Errors to poles of bedding, showing close correspondence with field measurements (squares) and the orientation of maximum errors in dip.

610 traced; these beds are individually well-resolved and generally steeper than the beds of 2 and 3.
611 These measurements closely correspond to field measurement b in dip but suggest a strike $\sim 5^\circ$ to
612 the west. Since several remotely-sensed beds agree closely, this rotation may be caused by a slight
613 error in field measurement.

614 Beds in 5 were measured in a second cliff-forming dolomite interval, and extracted error dis-
615 tributions overlap the field measurement c within the same interval, suggesting orientation re-
616 construction to within a few degrees. Field measurements d , e , and f were measured on a float-
617 covered slope of the Lemoenputs Formation with few traceable bedding planes. One somewhat
618 resistant dolomite bed (6) can be traced on both sides of the hillslope but not over its nose. When
619 grouped, these measurements outline a single plane dipping at $\sim 45^\circ$ that corresponds closely in
620 orientation to d , e , and f .

621 Bedding orientations extracted from the UAV dataset correspond closely to field-measured
622 orientations, recording bedding dips $30\text{-}50^\circ$ northwest (into the hillslope) and steepening with
623 elevation. In general, strike is constrained to within a few degrees, while dips are constrained to
624 within $\sim 5\text{-}15^\circ$. This error structure is consistent with the relatively stronger constraints on appar-
625 ent dips along the cliff face than dips in and out of the cliff. Flights on a single side of a relatively
626 planar outcrop entail little 3D structure with which to derive well-constrained orientations. How-
627 ever, even with a relatively low-resolution (15 cm/pixel) SfM photogrammetric elevation model,
628 the crucial observation of beds steeply dipping into the outcrop is easily captured.

629 **5 Potential future improvements to the statistical framework**

630 **5.1 Modeling data with different error structures**

631 The statistical error bounds developed for unweighted PCA regression in Section 3.3 are general
632 and adaptable to a wide variety of data types. Different statistical frameworks can be substi-
633 tuted, and supplements to this statistical framework can be used to model errors for uncertain
634 orientations using situation-specific information as described below.

635 **5.1.1 Adding a noise floor** PCA-based regression is responsive to the scale of errors, but known
636 errors in the input data are not automatically accounted for in the fitting process. If data input
637 error is independently measured, a “noise floor” can be imposed that defines a minimum amount
638 of noise expected for the input dataset. This can be accomplished by conditionally replacing λ_3 in
639 Equation 25 with a standard value for the minimum noise variance, to ensure that $\lambda_3 \geq \min \sigma_M^2$.

640 For instance, if the accuracy of a point cloud is 1 m, as computed based on external criteria
641 (e.g. the input stereo geometry of a gridded elevation model or measurement error for LIDAR or
642 radar ranging), introducing a noise floor of $\min \sigma_M^2 = 1$ into calculations of the noise covariance
643 could correct for false certainty arising from possible local smoothing.

644 **5.1.2 Rescaling error sensitivity** An advantage of the isotropic error framework of PCA is its
645 flexibility: because coordinates are not fixed, the input dataset can be rescaled along any axis.
646 Different axial weightings can be a useful way to incorporate known errors on single-axis param-
647 eters of the input data (e.g. photogrammetric image-registration errors). This property can be
648 used to control the relative sensitivity of the fit to errors along each axis of the input data. It
649 is often desirable to set error sensitivities separately based on informed criteria around dataset-
650 specific error sources (*Carroll and Ruppert, 1996*). For instance, orbital photogrammetric DEMs
651 might be tuned for chiefly vertical errors, while oblique SfM photogrammetry would be given
652 higher sensitivity in the oblique view direction. While our current statistical framework treats
653 errors along all axes equally, the software can be modified to fit different errors along each axis.
654 The PCA framework can be limited to only vertical errors, mimicking OLS, or utilized in a variety
655 of other weighted schemes (e.g. *Friendly et al., 2013; Francq and Govaerts, 2014*).

656 **5.1.3 Applying other statistical models** Numerical methods such as bootstrap resampling and
657 Monte Carlo sensitivity analysis can be substituted for the asymptotic Gaussian and noise-based
658 statistical models described in this paper [Section 3.3.4]. Although these numerical methods are
659 computationally intensive and difficult to generalize, they allow the incorporation of detailed as-
660 sumptions about dataset errors, and can support situation-specific, high-quality errors in the fit
661 parameters of the plane. Additionally, a variety of regression techniques with different assump-
662 tions, such as OLS and weighted schemes, can be substituted for PCA [Section 3.1.1]. No matter
663 which statistical framework is used, the fitting and data-visualization methods outlined in this
664 paper can be used to represent the resulting uncertain planes.

665 **5.2 The link with Bingham statistics**

666 The Bingham statistical distribution is a generalized statistical distribution of undirected orienta-
667 tions defined in spherical space (*Bingham, 1974*). The core assumption of the Bingham framework
668 is that for the axes of a distribution \mathbf{a} , $\text{trace}(\mathbf{a}^2) = 1$. Applying the Bingham transformation to a
669 Cartesian set of error axes is functionally equivalent to finding the tangents to a hyperbolic error
670 range. As such, our hyperbolic axes \mathbf{h} can be transformed into the Bingham structural parameters
671 κ_1 and κ_2 (*Bingham, 1974; Onstott, 1980*).

672 When fully explored, the formal link between PCA regression and Bingham statistics will allow
673 uncertain orientation measurements to be treated as probability density functions in spherical
674 space. This will allow higher-level statistical transforms to be applied to measurements, including
675 combination using error-propagation techniques, and the application of statistical significance
676 tests. Formalizing the conceptual link between Cartesian and Bingham statistics may unlock new
677 potential applications for this error-analysis framework.

678 **6 Conclusion and recommendations**

679 We have described a complete error-analysis workflow for the orientation of geological planes, es-
680 pecially stratigraphic bedding, that improves on typical regression statistics for the assessment of
681 geological planes. Our PCA-based analytical approach includes a regression method, a framework
682 for statistically-based errors, mathematical approaches for the 2D visualization and reporting of
683 structural data with errors, and software to handle calculations and data management.

684 As shown by the two terrestrial examples, these analytical procedures are generalized and
685 flexible. They can be used to model the orientation of planes on map-projected satellite and aerial
686 imagery, as well as digital surface models built with LIDAR, UAV photogrammetry, and radar
687 techniques. Application of the error analysis method in the San Rafael Swell successfully captures
688 the structural pattern of this geological area. Relatively good conformance with in-situ measure-
689 ments was gained despite the use of off-the-shelf data products, reflecting the flexibility and wide
690 applicability of this method to readily available nadir-looking imagery and elevation datasets.
691 Application of the method to oblique-looking UAV data on the Naukluft plateau demonstrated
692 the viability of PCA-based orientation calculation in a reconnaissance study using high-obliquity
693 aerial imagery with relatively inexpensive equipment and SfM photogrammetry software.

694 The coupling of a robust error-analysis framework with techniques to visualize the error space
695 allows simple and transparent analytical workflows. Error-minimizing data collection strategies
696 can be easily compared, and heterogeneous data can be used with full knowledge of the errors
697 involved. We propose a standardized method for numerical reporting of uncertain planar orien-
698 tations, combining the basic strike/dip representation with terms for angular errors on two axes,
699 and the rake of these error axes within the best-fitting plane [Section 2], and yielding [*strike*,
700 *dip*, *rake*, *min. angular error*, *max. angular error*] for each measurement. Additionally, we create
701 intuitive stereonet display methods that provide a natural means to visualize uncertain planar
702 orientations alongside traditional structural data.

703 Overall, the results of this study suggest that errors arising from outcrop geometry are at
704 least as important as precision of the input remote-sensing dataset in defining the error space of
705 a fitted plane. Traces of geologic features can only be modeled as unique planes when they query
706 a three-dimensional point dataset, and outcrops within the same dataset can have completely
707 different error structures. For characterization of orientations in an outcrop, we recommend
708 that care be taken to find beds that sample a wide range of hillslope aspect or depth within an
709 obliquely-measured scene (or groups of closely-spaced beds that collectively sample such a range).
710 Furthermore, we suggest that digitizing precision is of subsidiary importance to collecting such
711 a varied sample set: small errors in describing a fitted plane are will not significantly diminish
712 the quality of the fit relative to poor sampling of three-dimensional outcrop variability. Thus,
713 measuring a large quantity of adjacent bed surfaces provides the best opportunity to remove poor
714 measurements and group incomplete ones.

715 We expect the methods described here will push the scale of geologic inference towards the
716 resolution limit of 3D surface models, broadening the range of structural interpretations that can
717 be made from remotely sensed imagery. This will increase the fidelity of structural measurements
718 supported by UAVs and LIDAR scanners in terrestrial research, rover-based cameras for *in-situ*
719 planetary exploration, and satellite data for regional planetary mapping. To that end, we release
720 software to implement these methods and visualize strike and dip in Appendix B.

721 **7 Acknowledgements**

722 We would like to thank NASA for the NASA Earth and Space Science Fellowship to D.P. Quinn
723 that funded this work. Our software tools are archived with CaltechDATA (*DOI not yet created*) in
724 conjunction with this work. Data for the examples shown in the paper is part of the testing suite
725 for the attitude software package.

Bibliography

- Babamoradi, H., F. Van Den Berg, and A. Rinnan (2013), Bootstrap based confidence limits in principal component analysis - A case study, *Chemometrics and Intelligent Laboratory Systems*, 120, 97–105, doi:10.1016/j.chemolab.2012.10.007.
- Bingham, C. (1974), An Antipodally Symmetric Distribution on the Sphere, *The Annals of Statistics*, 2(6), 1201–1225, doi:10.1214/aos/1176342874.
- Buckley, S. J., J. Howell, H. Enge, and T. Kurz (2008), Terrestrial laser scanning in geology: Data acquisition, processing and accuracy considerations, *Journal of the Geological Society*, 165(3), 625–638, doi:10.1144/0016-76492007-100.
- Carroll, R. J., and D. Ruppert (1996), The Use and Misuse of Orthogonal Regression in Linear Errors-in-Variables Models, *The American Statistician*, 50(1), 1–6, doi:10.1080/00031305.1996.10473533.
- Cawood, A. J., C. E. Bond, J. A. Howell, R. W. Butler, and Y. Totake (2017), LiDAR, UAV or compass-clinometer? Accuracy, coverage and the effects on structural models, *Journal of Structural Geology*, 98, 67–82, doi:10.1016/j.jsg.2017.04.004.
- Cruden, D. M., and H. A. K. Charlesworth (1976), Errors in strike and dip measurements, *Bulletin of the Geological Society of America*, 87(7), 977–980, doi:10.1130/0016-7606(1976)87<977:EISADM>2.0.CO;2.
- DiBiase, R. A., A. B. Limaye, J. S. Scheingross, W. W. Fischer, and M. P. Lamb (2013), Deltaic deposits at Aeolis Dorsa: Sedimentary evidence for a standing body of water on the northern plains of Mars, *Journal of Geophysical Research: Planets*, 118(6), 1285–1302, doi:10.1002/jgre.20100.
- Doelling, H., P. Kuehne, G. Willis, and J. Ehler (2017), Geologic map of the San Rafael Desert 30' x 60' quadrangle, Emery and Garfield Counties, Utah.
- Dromart, G., C. Quantin, and B. Olivier (2007), Stratigraphic architectures spotted in southern Melas Chasma, Valles Marineris, Mars, *Geology*, 35(4), 363–366, doi:10.1130/G23350A.1.
- Edgar, L., J. P. Grotzinger, A. G. Hayes, D. M. Rubin, S. W. Squyres, J. F. Bell, and K. E. Herkenhoff (2012), Stratigraphic architecture of bedrock reference section, Victoria crater, Meridiani Planum, Mars, in *Sedimentary Geology of Mars*, edited by J. P. Grotzinger and R. E. Milliken, SEPM (Society for Sedimentary Geology), doi:10.2110/pec.12.102.
- Faber, K., and B. R. Kowalski (1997), Propagation of measurement errors for the validation of predictions obtained by principal component regression and partial least squares, *Journal of Chemometrics*, 11(3), 181–238, doi:10.1002/(SICI)1099-128X(199705)11:3<181::AID-CEM459>3.0.CO;2-7.
- Faber, N. M., L. Buydens, and G. Kateman (1993), Standar Errors in the Eigenvalues of a Cross-Product Matrix: Theory and Applications, *Journal of Chemometrics*, 7, 495–526, doi:10.1063/1.3033202.
- Faber, N. M., M. J. Meinders, P. Geladi, M. Sjöström, L. M. C. Buydens, and G. Kateman (1995), Random error bias in principal component analysis. Part I. derivation of theoretical predictions, *Analytica Chimica Acta*, 304(3), 257–271, doi:10.1016/0003-2670(94)00585-A.
- Fahrmeir, L., T. Kneib, S. Lang, and B. Marx (2013), *Regression: Models, Methods, and Applications*, Springer-Verlag, Berlin Heidelberg.
- Fienen, M. N. (2005), The Three-Point Problem , Vector Analysis and Extension to the N-Point Problem, *Journal of Geoscience Education*, 53(3), 257–263, doi:10.131402110716480.
- Fisher, N. I., T. Lewis, and B. J. Embleton (1987), *Statistical Analysis of Spherical Data*, Cambridge university press.
- Fraeman, A. A., R. E. Arvidson, J. G. Catalano, J. P. Grotzinger, R. V. Morris, S. L. Murchie, K. M. Stack, D. C. Humm, J. a. McGovern, F. P. Seelos, K. D. Seelos, and C. E. Viviano (2013), A hematite-bearing layer in Gale Crater, Mars: Mapping and implications for past aqueous conditions, *Geology*, 41(10), 1103–1106, doi:10.1130/G34613.1.
- Francoq, B. G., and B. B. Govaerts (2014), Hyperbolic confidence bands of errors-in-variables regression lines applied to method comparison studies, *Journal de la Société Française de Statistique*, 155(1), 23–45.
- Friendly, M., G. Monette, and J. Fox (2013), Elliptical Insights: Understanding Statistical Methods through Elliptical Geometry, *Statistical Science*, 28(1), 1–39, doi:10.1214/12-STS402.
- Gesch, D. B., M. J. Oimoen, and G. A. Evans (2014), Accuracy assessment of the US Geological Survey National Elevation Dataset, and comparison with other large-area elevation datasets: SRTM and ASTER, *Tech. rep.*, US Geological Survey.
- Gilluly, J., and J. B. Reeside Jr (1928), Sedimentary rocks of the San Rafael Swell and some adjacent areas in eastern

- Utah, *Tech. Rep. 150-D*, US Geological Survey.
- Goudge, T. A., R. E. Milliken, J. W. Head, J. F. Mustard, and C. I. Fassett (2017), Sedimentological evidence for a deltaic origin of the western fan deposit in Jezero crater, Mars and implications for future exploration, *Earth and Planetary Science Letters*, 458, 357–365, doi:10.1016/j.epsl.2016.10.056.
- Jolliffe, I. T. (2002), Principal Component Analysis, *Springer Series in Statistics*, 98, 487, doi:10.1007/b98835.
- Kent, J., J. Briden, and K. Mardia (1983), Linear and planar structure in ordered multivariate data as applied to progressive demagnetization of palaeomagnetic remanence, *Geophysical Journal of the Royal Astronomical Society*, 75(3), 593–621, doi:10.1111/j.1365-246X.1983.tb05001.x.
- Kirschvink, J. L. (1980), The least-squares line and plane and the analysis of paleomagnetic data, *Geophysical Journal of the Royal Astronomical Society*, 62(3), 699–718, doi:10.1111/j.1365-246X.1980.tb02601.x.
- Kite, E. S., K. W. Lewis, M. P. Lamb, C. E. Newman, and M. I. Richardson (2013), Growth and form of the mound in Gale Crater, Mars: Slope wind enhanced erosion and transport, *Geology*, 41(5), 543–546, doi:10.1130/G33909.1.
- Kite, E. S., J. Sneed, D. P. Mayer, K. W. Lewis, T. I. Michaels, A. Hore, and S. C. Rafkin (2016), Evolution of major sedimentary mounds on Mars: Buildup via anticompensational stacking modulated by climate change, *Journal of Geophysical Research: Planets*, 121(11), 2282–2324, doi:10.1002/2016JE005135.
- Lewis, K., O. Aharonson, and J. Grotzinger (2008a), Quasi-Periodic Bedding in the Sedimentary Rock Record of Mars, *Science*, 1532(2008), doi:10.1126/science.1161870.
- Lewis, K. W., and O. Aharonson (2006), Stratigraphic analysis of the distributary fan in Eberswalde crater using stereo imagery, *Journal of Geophysical Research*, 111(E6), 1–7, doi:10.1029/2005JE002558.
- Lewis, K. W., and O. Aharonson (2014), Occurrence and origin of rhythmic sedimentary rocks on Mars, *Journal of Geophysical Research: Planets*, 119(6), 1432–1457, doi:10.1002/2013JE004404.
- Lewis, K. W., O. Aharonson, J. P. Grotzinger, S. W. Squyres, J. F. Bell, L. S. Crumpler, and M. E. Schmidt (2008b), Structure and stratigraphy of home plate from the spirit mars exploration rover, *Journal of Geophysical Research: Planets*, 113(E12).
- Malin, M. C., and K. S. Edgett (2000), Sedimentary Rocks of Early Mars, *Science*, 290(5498), 1927–1937, doi:10.1126/science.290.5498.1927.
- Malinowski, E. (1977), Theory of error in factor analysis, *Analytical Chemistry*, 49(4), 606–612, doi:10.1021/ac50012a026.
- Mardia, K. V. (2014), *Statistics of Directional Data*, Academic press.
- McEwen, A. S., M. C. Malin, M. H. Carr, and W. K. Hartmann (1999), Voluminous volcanism on early Mars revealed in Valles Marineris, *Nature*, 397(6720), 584–586, doi:10.1038/17539.
- Metz, J., J. Grotzinger, C. Okubo, and R. Milliken (2010), Thin-skinned deformation of sedimentary rocks in Valles Marineris, Mars, *Journal of Geophysical Research E: Planets*, 115(11), 1–28, doi:10.1029/2010JE003593.
- Nurunnabi, A., D. Belton, and G. West (2012), Diagnostic-robust statistical analysis for local surface fitting in 3D point cloud data, *ISPRS Annals of the Photogrammetry Remote Sensing and Spatial Information Sciences*, I-3(September), 269–274, doi:10.5194/isprsannals-I-3-269-2012.
- Okubo, C. H. (2010), Structural geology of Amazonian-aged layered sedimentary deposits in southwest Candor Chasma, Mars, *Icarus*, 207(1), 210–225, doi:10.1016/j.icarus.2009.11.012.
- Okubo, C. H., K. W. Lewis, A. S. McEwen, and R. L. Kirk (2008), Relative age of interior layered deposits in southwest Candor Chasma based on high-resolution structural mapping, *Journal of Geophysical Research*, 113(E12), E12,002, doi:10.1029/2008JE003181.
- Onstott, T. (1980), Application of the Bingham distribution function in paleomagnetic studies, *Journal of Geophysical Research: Solid Earth*, 85(B3), 1500–1510, doi:10.1029/JB085iB03p01500.
- Quantin, C., P. Allemand, N. Mangold, G. Dromart, and C. Delacourt (2005), Fluvial and lacustrine activity on layered deposits in Melas Chasma, Valles Marineris, Mars, *Journal of Geophysical Research E: Planets*, 110(12), 1–18, doi:10.1029/2005JE002440.
- Quinn, D. P., and B. L. Ehlmann (2018), The deposition and alteration history of the northeast Syrtis layered sulfates, *Journal of Geophysical Research: Planets*, (submitted).
- Quinn, D. P., and J. P. Grotzinger (2016), Stratigraphy and sedimentology of the Zebra Nappe, Naukluft Nappe Complex, Namibia, *Geological Society of America Abstracts with Programs*, 48(7), doi:10.1130/abs/2016AM-287992.

- Richter-Gebert, J. (2011), Conics and their duals, in *Perspectives on Projective Geometry: A Guided Tour Through Real and Complex Geometry*, pp. 145–166, Springer Berlin Heidelberg, Berlin, Heidelberg, doi:10.1007/978-3-642-17286-1_9.
- Rowe, C. D., A. Fagereng, J. a. Miller, and B. Mapani (2012), Signature of coseismic decarbonation in dolomitic fault rocks of the Naukluft Thrust, Namibia, *Earth and Planetary Science Letters*, 333-334, 200–210, doi:10.1016/j.epsl.2012.04.030.
- Schröcker, H.-P. (2007), Minimal Enclosing Hyperbolas of Line Sets, *Contributions to Algebra and Geometry*, 48(2), 367–381.
- Stack, K. M., C. S. Edwards, J. P. Grotzinger, S. Gupta, D. Y. Sumner, F. J. Calef, L. A. Edgar, K. S. Edgett, A. A. Fraeman, S. R. Jacob, L. Le Deit, K. W. Lewis, M. S. Rice, D. Rubin, R. M. E. Williams, and K. H. Williford (2015), Comparing orbiter and rover image-based mapping of an ancient sedimentary environment, Aeolis Palus, Gale crater, Mars, *Icarus*, 280, 3–21, doi:10.1016/j.icarus.2016.02.024.
- Tipping, M. E., and C. M. Bishop (1999), Mixtures of probabilistic principal component analyzers., *Neural computation*, 11(2), 443–482, doi:10.1162/089976699300016728.
- Vollgger, S. A., and A. R. Cruden (2016), Mapping folds and fractures in basement and cover rocks using UAV photogrammetry, Cape Liptrap and Cape Paterson, Victoria, Australia, *Journal of Structural Geology*, 85, 168–187.
- Weingarten, J., G. Gruener, and R. Siegwart (2004), Probabilistic plane fitting in 3D and an application to robotic mapping, *IEEE International Conference on Robotics and Automation*, 1(April), 927–932, doi:10.1109/ROBOT.2004.1307268.

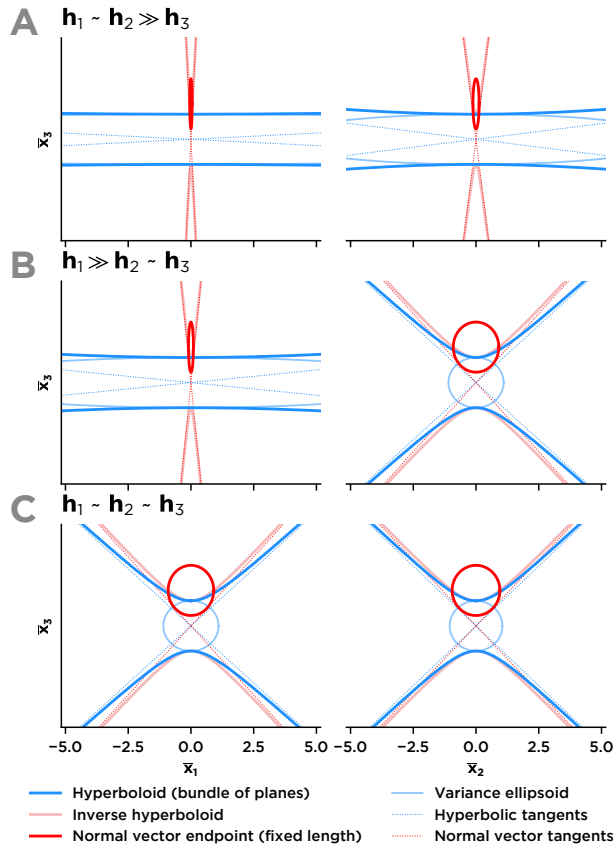


Figure 14: Several mathematically related constructions of the error space of an uncertain plane as hyperbolic quadrics and ellipsoids. Correspondence of the error space of a plane defined by semiaxes \mathbf{h} with hyperbolic and ellipsoidal representations of the error space of the normal vector to the plane, showing angular scaling of the subtended area of these constructions depending on the ratio of the semiaxes.

Appendices

1 A Quadric representation of the orientation error space

2 We represent error surfaces for planar orientation measurements as 3D generalized conic sections, or quadric surfaces [Figure 2]. Planar fit errors can be represented as matrices, plotted as quadrics, and translated between representations of the error space as hyperboloids, ellipsoids, and cones of tangency by linear algebraic methods, such as the geometric (e.g. affine and projective) transformations described below.

7 In three-dimensional space, an uncertain planar measurement is structured as a hyperboloid of two sheets (an elliptic hyperboloid), opening along the error axis (λ_3). Conceptually, this hyperboloid represents the minimal enclosing surface of a bundle of all possible planes corresponding to the regression (Schröcker, 2007). Another possible representation is as a bundle of possible normal vectors to the plane, which can be defined by a hyperboloid encompassing all vectors or an ellipsoid containing the endpoints of equal-length vectors [Figure 1]. Representation of errors in a normal-vector framework is less inherently meaningful than the hyperbolic construction, since normal vectors do not “contain” the modeled plane. However, the manipulation of uncertain vectors is simpler than uncertain planar bundles, and the vector representation of orientation errors

16 eases comparison and transformation [Figure 14].

17 **A.1 A hyperboloid enclosing the plane**

18 The axes h define a hyperboloid representing the errors to the planar fit, conforming to the general
19 equation for an origin-centered hyperbola opening along \bar{x}_3 of

$$\frac{\bar{x}_1^2}{h_1^2} + \frac{\bar{x}_2^2}{h_2^2} - \frac{\bar{x}_3^2}{h_3^2} = -1. \quad (38)$$

20 When incorporated into a 4×4 matrix representation of the PCA-aligned error quadric,

$$\bar{\mathbf{Q}}_{\mathbf{H}} = \text{diag}\left(\left[\frac{1}{h_1^2}, \frac{1}{h_2^2}, -\frac{1}{h_3^2}, -1\right]\right), \quad (39)$$

21 forms part of a general equation for a quadric surface

$$\bar{\mathbf{x}}^T \bar{\mathbf{Q}}_{\mathbf{H}} \bar{\mathbf{x}} = 0 \quad (40)$$

22 (e.g. *Richter-Gebert*, 2011).

23 This matrix representation allows manipulation of the error distribution in three dimensions.
24 For example, the PCA-aligned error hyperboloid can be transformed into real space by sequen-
25 tially applying two affine transformations to $\bar{\mathbf{Q}}_{\mathbf{H}}$: first a rotation into the real coordinate vectors
26 with the augmented rotation matrix \mathbf{V}_A (\mathbf{V} augmented with the 4×4 identity matrix) and trans-
27 lation defined by \mathbf{T}_μ , an identity matrix with a last column $[-\mu_D, 1]$, to shift the center of the
28 coordinate system to the origin from the mean of the measured plane. Thus,

$$\mathbf{Q}_{\mathbf{H}} = (\mathbf{V}_A \mathbf{T})^T \bar{\mathbf{Q}}_{\mathbf{H}} \mathbf{V}_A \mathbf{T}, \quad (41)$$

29 and the quadric representing the uncertain plane becomes

$$\mathbf{x}^T \mathbf{Q}_{\mathbf{H}} \mathbf{x} = 0. \quad (42)$$

30 **A.2 Errors to normal vectors**

31 Errors to normal vectors can be defined as both a hyperboloid containing all possible normal
32 vectors passing through the center of the plane, and an offset ellipsoid representing errors to a
33 normal vector with fixed length. Projected from the origin, all error spaces for the normal vector
34 subtend the same angle, equivalent but orthogonal to that subtended by $\bar{\mathbf{Q}}_{\mathbf{H}}$ [Figure 14].

35 The hyperbolic formulation of normal-vector errors is the “dual” quadric surface to $\bar{\mathbf{Q}}_{\mathbf{H}}$, re-
36 lated by inversion:

$$\bar{\mathbf{Q}}'_{\mathbf{H}} = \bar{\mathbf{Q}}_{\mathbf{H}}^{-1} = \text{diag}([h_1^2, h_2^2, -h_3^2, -1]). \quad (43)$$

37 This defines a hyperboloid of two sheets with a cone of tangency spanning the same angular dis-
 38 tance as $\overline{\mathbf{Q}}_{\mathbf{H}}$, but normal to it. The hyperboloid defining normal vector error is a *point quadric*,
 39 dual to the hyperbolic *plane quadric* surrounding the nominal value of the plane. Duality is a gen-
 40 eralization of the concept of “inversion poles”, which shows that for a given conic section, any
 41 interior point (a “pole”) can be related to a unique reciprocal line outside the conic (a “polar”)
 42 (*Richter-Gebert*, 2011).

43 A more intuitive ellipsoidal representation of the normal vector error space is arrived at when
 44 a fixed-length normal vector is assumed. Normal vector errors can be defined as an ellipsoid with
 45 semiaxes proportional to $\frac{1}{h_i^2}$ and an arbitrary scale. For a normal vector of length $\sqrt{2}h_3$, the
 46 ellipsoid semiaxes are scaled by a factor of h_3^2 , resulting in an ellipsoid with major axes $[\frac{h_3^2}{h_1^2}, \frac{h_3^2}{h_2^2}, h_3]$
 47 with a center offset $\sqrt{2}h_3$ from the origin along the 3 axis. This construction of the normal vector
 48 errors keeps the same relationship with the angular tangents to the normal vectors [Figure 14].

49 **A.3 General method to map a quadric to a conic**

50 Quadric surfaces can be sliced in any plane to form a 2D conic section. The ability to transform
 51 and slice the matrix representation of the error space along arbitrary axes allows the plotting of
 52 planar errors to single or multiple planes into common Cartesian coordinates for projection along
 53 arbitrary view axes [Figure 13].

54 Using a plane defined by two perpendicular vectors \mathbf{v}_1 and \mathbf{v}_2 , and a point \mathbf{a} within the plane,
 55 we can define a 4×3 transformation matrix to map the quadric down to a 2D conic section,
 56 stacking these vectors as columns, augmented with a final row $k = [0, 0, 1]$:

$$\mathbf{T} = \begin{bmatrix} \mathbf{v}_1 & \mathbf{v}_2 & \mathbf{a} \\ 0 & 0 & 1 \end{bmatrix}. \quad (44)$$

57 The conic section

$$\mathbf{C}_{\mathbf{H}} = \mathbf{T}^T \mathbf{Q}_{\mathbf{H}} \mathbf{T} \quad (45)$$

58 defines the slice of the error space along that plane. The mapping to a hyperbolic slice of the error
 59 hyperboloid at any angle γ within the fitted plane can be found using the transformation matrix
 60 for axes $\overline{\mathbf{x}}_{\gamma} = [\cos \gamma, \sin \gamma, 0]$ and $\overline{\mathbf{x}}_3 = [0, 0, 1]$:

$$\mathbf{T} = \begin{bmatrix} \cos \gamma & 0 & 0 \\ \sin \gamma & 0 & 0 \\ 0 & 1 & 0 \\ 0 & 0 & 1 \end{bmatrix}. \quad (46)$$

61 For the simple case of the slice of the error space aligned with $\overline{\mathbf{x}}_1 = [1, 0, 0]$ and $\overline{\mathbf{x}}_3 = [0, 0, 1]$ and

62 centered at the origin, a transformation matrix

$$\mathbf{T} = \begin{bmatrix} 1 & 0 & 0 \\ 0 & 0 & 0 \\ 0 & 1 & 0 \\ 0 & 0 & 1 \end{bmatrix} \quad (47)$$

63 resolves

$$\mathbf{C}_H = \mathbf{T}^T \overline{\mathbf{Q}}_H \mathbf{T} = \text{diag}([\frac{1}{h_1^2}, -\frac{1}{h_3^2}, 1]), \quad (48)$$

64 a hyperbola of two sheets, opening along h_3 .

65 **A.4 General method to move to spherical coordinates**

66 A general representation for the tangents to the hyperbolic error spaces discussed above can be
67 constructed as a cone of tangency, which can be easily transformed into spherical coordinates.

68 This elliptic cone has the same semiaxes as the elliptic hyperboloid \mathbf{Q}_H and can be represented as

69

$$\overline{\mathbf{Q}}_T = \text{diag}([\frac{1}{h_1^2}, \frac{1}{h_2^2}, -\frac{1}{h_3^2}, 0]) \quad (49)$$

70 (with the last -1 in $\overline{\mathbf{Q}}_H$ replaced with a 0). The orthogonal angular cone defining the normal

71 vector can be found in general by inverting the cone of tangents $\overline{\mathbf{Q}}_T$ to form

$$\overline{\mathbf{Q}}_N = \text{diag}([h_1^2, h_2^2, -h_3^2, 0]). \quad (50)$$

72 **B Software tools**

73 We provide a software implementation that supports the orientation-analysis statistics and vi-
74 sualizations described here. The core software is the `attitude` Python module, which contains
75 regression code and functions for importing point-based bedding traces from GIS data and other
76 formats. This package also contains methods for plotting uncertain orientations in spherical coor-
77 dinates using the Python libraries `matplotlib` and `cartopy`. The `attitude` module also includes
78 a Javascript component implementing tools based on the `d3` visualization library for interactive
79 stereonet and plots of decomposed axial variance. The Python and Javascript components can
80 be used together in the **iPython Notebook** analytical environment, allowing interactive data in-
81 spection and exploratory grouping of jointly fitted planes, with minimal setup [Figure 15a]. The
82 `attitude` module is open-source and available on GitHub (<https://github.com/davenquinn/Attitude>).
83 Documentation and example notebooks are available at <https://github.io/davenquinn/Attitude>.
84 Version 1.0 of the software and documentation has been archived with CaltechDATA in conjunc-
85 tion with this publication.

86 The `Orienteer` software application [Figure 15b] was created to ease the management of ori-

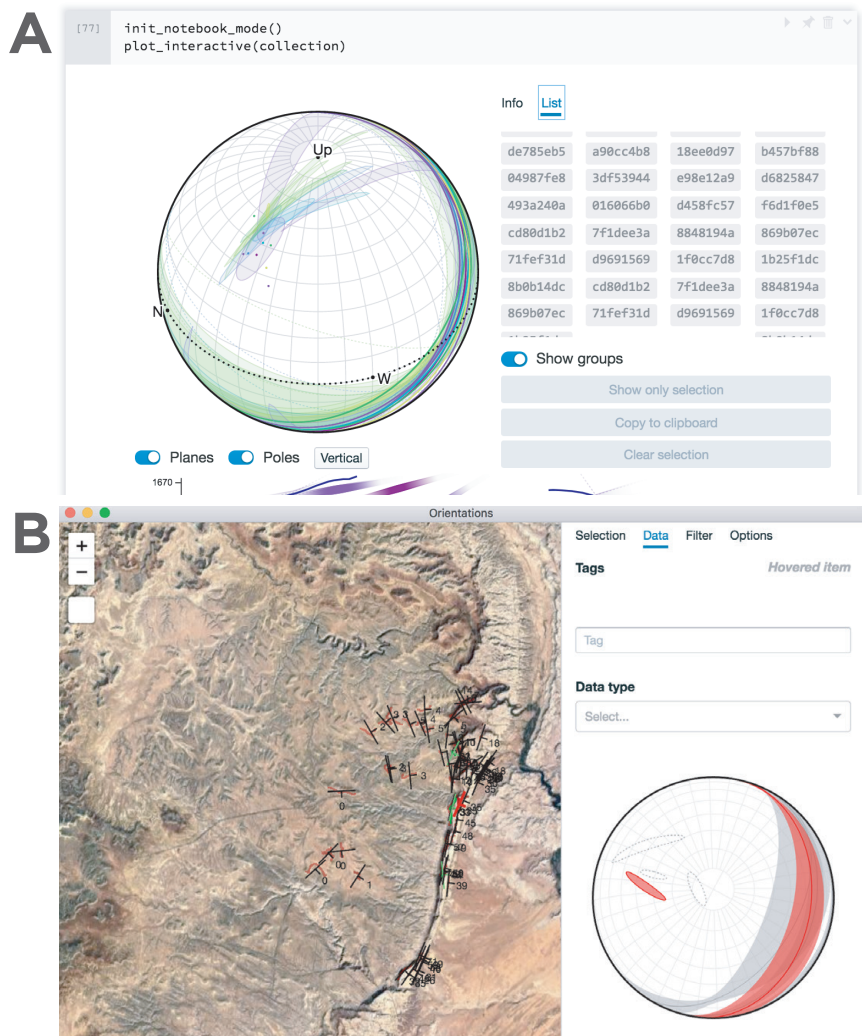


Figure 15: Screenshots of software developed in this study. (a) The attitude Python module running in an *iPython* notebook. (b) The *Orienteer* application in use for filtering a database of orientations atop Google Maps data for the San Rafael Swell, Utah.

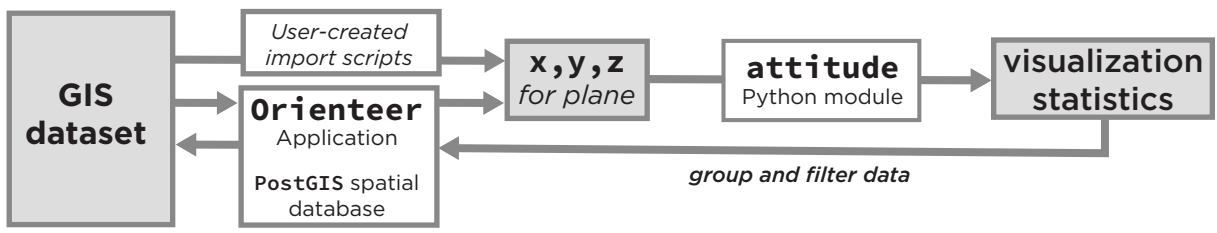


Figure 16: Workflow diagram showing the roles of the attitude Python module and Orienteer data-management application in an orientation-measurement software project. The attitude module supports a linear process flow, while the Orienteer application enables the management of orientation data across a large mapping project.

87 entation data over a large mapping project. This cross-platform desktop application interfaces
88 with the attitude module and supports the management of orientation measurements and their
89 underlying raster elevation models in a PostGIS spatial database. This application eases the filter-
90 ing of planes by quality and grouping and splitting to assess the viability of joint fitting for data re-
91 duction, and serves as a companion to GIS software [Figure 16]. Although Orienteer adds pow-
92 erful data management capabilities to the attitude software, it is more difficult to set up, requir-
93 ing a PostgreSQL server, and is somewhat unstable due to its relative complexity. This applica-
94 tion is also open-source and is available on GitHub (<https://github.com/davenquinn/Orienteer>)
95 as well as archived with CaltechDATA in conjunction with publication.

96 The statistical method developed here can be expressed with basic linear algebra and should
97 be straightforward to implement in programming environments such as MATLAB or R. Test cases
98 are provided with the attitude module that can be used to verify accuracy. Additionally, since
99 both QGIS and ArcGIS expose Python bindings, it is possible to use the attitude module directly
100 within standard GIS software.